Master's Thesis

UWB Radio Channel Analysis Using the SAGE Algorithm

Katharina Hausmair

Signal Processing and Speech Communication Laboratory
Graz University of Technology
Head: Univ.-Prof. DI Dr. techn. Gernot Kubin

Supervisor/Assessor: DI Dr. Assoc.Prof. Klaus Witrisal

Graz, March 2010

STATUTORY DECLARATION

I declare that I have authored this thesis independently, that I have not used other than the declared sources / resources, and that I have explicitly marked all material which has been quoted either literally or by content from the used sources.

Graz, ...

Date (Signature)

Abstract

In this thesis a simple time gating extension to the wideband SAGE algorithm is proposed to make the algorithm suitable for time domain estimation of delays, azimuth angles, elevation angles and complex amplitudes of deterministic MPCs in UWB radio channels.

The algorithm is applied to channel measurement data. Analysis of the results shows that the approach is capable of identifying individual impinging waves. It is demonstrated that the channel can be approximated quite well by reconstruction of the received signals with the estimated wave parameters. An illustration of the detected MPCs as a function of antenna displacement suggests path tracking potential.

From the obtained results can be concluded that the performance of the proposed algorithm is heavily dependent on the channel characteristics, as well as the choice of antenna array configuration.

The algorithm delivers satisfying results for all of the considered bandwidths, which leaves the ultimate choice of bandwidth open to meet other demands of particular applications.

Kurzfassung

In der vorliegenden Arbeit wird der konventionelle Breitband-SAGE Algorithmus mit einem einfachen Time-Gating Ansatz erweitert. Diese Erweiterung ermöglicht es, den Algorithmus für präzise Schätzung von Zeitverzögerungen, Breitenwinkeln, Höhenwinkeln und komplexen Amplituden deterministischer Multipath-Komponenten in UWB-Funkkanälen einzusetzen.

Mit dem vorgeschlagenen Algorithmus werden Messdaten analysiert. Die Ergebnisse zeigen, dass der erweiterte SAGE-Algorithmus individuelle Multipath-Komponenten identifizieren kann. Es wird demonstriert, dass mit den Ergebnissen eine gute Annäherung an den tatsächlichen Kanal erreicht wird. Die Darstellung der Bewegung ermittelter Komponenten als Funktion der Antennenposition lässt Path-Tracking Potential vermuten.

Aus den erzielten Resultaten lässt sich schließen, dass die Leistung des Algorithmus stark von den Kanaleigenschaften und der gewählten Antennengruppenkonfiguration abhängig ist.

Da der Algorithmus für alle berücksichtigten Bandbreiten brauchbare Ergebnisse liefert, kann bei der Wahl der Bandbreite auf Anforderungen möglicher Anwendungen Rücksicht genommen werden.

Acknowledgements

I would like to take the opportunity to thank the people who made this thesis possible.

I especially would like to thank my supervisor, Dr. Klaus Witrisal, for his great support, encouragement and patience during my thesis. In addition to his ideas and professional advice, his enthusiasm and perpetual motivation helped to make research fun for me. I simply could not have wished for a better advisor.

Thanks to my colleagues Paul Meissner, Christoph Steiner and Georg Kail, who contributed important ideas that helped steer my work in the right direction.

Lastly, and most importantly, I would like to thank my entire family and Beni for supporting me in every possible way throughout my studies at University.

Contents

Chapter 1

Introduction

1.1 Motivation and Goal

Ultra–wideband (UWB) radio systems are defined by the use of signal bandwidths of 500MHz or more. Since such large bandwidths offer many advantages, these systems have become popular for a wide range of applications. For communication systems, UWB provides high data rates and robustness against small scale fading. Low power spectral density reduces interference with other systems. The excellent temporal resolution that comes with the use of large bandwidths enables the design of accurate ranging and positioning systems. Such systems require the extraction of location related information, like angles-of-arrival and delays of multipath components (MPCs), from the radio channel [GTG+05]. Hence, efficient methods are required to extract the parameters of interest from channel measurement data.

The goal of this thesis is to provide a simple and efficient method to extract parameters from UWB radio channels. For this purpose, the space alternating generalized expectation maximization (SAGE) algorithm, which is applied in [FDHT96] for time domain channel parameter estimation in wideband systems, is extended to achieve high accuracy in azimuth, elevation, delay and complex amplitude estimation of deterministic MPCs in UWB channels.

The approach proposed in this thesis assumes the received signal to be the sum of deterministic waves reaching the receiver at different delays from distinct angles. Array processing provides the necessary information to resolve the parameters of the MPCs in the estimation procedure, which relies on beamforming in combination with time gating and a matched filter.

1.2 Outline

Chapter 2 gives a short review of comparable parameter estimation approaches. In Chapter 3 of this thesis, the underlying signal model is defined. Chapter 4 at first discusses, why the problem at hand requires the use of more complex estimation procedures than a simple maximum likelihood estimation. Then, the expectation maximization (EM) algorithm, on which the SAGE algorithm is based on, is explained as well as the SAGE estimation procedure itself. The Chapter also includes a detailed description of the extension that is imperative to make the algorithm suitable for UWB channel parameter estimation. As the estimation of elevation angles can in some cases be neglected, signal model and estimation procedure are both designed to allow for inclusion and exclusion of elevation estimation. A detailed demonstration of the results obtained with the proposed algorithm for different measurement environments, bandwidth settings and antenna array sizes can be found in Chapter 5. Finally, the Conclusions of the thesis are presented in Chapter 6.

Chapter 2

Review of Comparable Research

Numerous publications concerning parameter estimation in UWB radio channels have appeared in the past decade. Publications that deal with characterization of the channel generally are focused on finding parameters like decay factors for statistical channel models such as the IEEE 802.15.3a standard model.

Publications that aim at providing information for ranging or positioning systems mainly concentrate on either estimating the times-of-arrival or the angles-of-arrival of MPCs, while only few publications concentrate on the combined extraction of delays and angles-of-arrival of MPCs. In most of these publications, the main goal is to extract the parameters of only the first component that arrives at the receiver.

Only few algorithms deal with the combined extraction of parameters of more than one MPC in UWB channels [Mol09] and are therefore comparable to this work:

Sensor-CLEAN The Sensor-CLEAN [CSW02] algorithm is an extension of the CLEAN algorithm, which was initially used to enhance radio-astronomical maps of the sky and has also been adapted to narrowband characterization problems [CSW02]. The Sensor-CLEAN assumes the received signal to be the sum of UWB pulses of unknown shape. It relies on delay-and-sum beamforming in combination with a relaxation window and successive cancellation techniques to estimate amplitudes, azimuth angles, elevation angles, delays and pulse shapes of deterministic MPCs.

Basically, at first delay-and-sum beamforming is performed combining received signals from a number of different antennas. Then, the entry with maximum magnitude in the beamformer output is determined. This entry represents the strongest MPC and its parameters. After canceling the contribution of the identified MPC and a relaxation window of a certain span around it from the data, the search for the next MPC starts

until the energy of a detected MPC falls below a predefined threshold.

Since UWB signals can suffer from severe distortions over different propagation paths, an advantage of the Sensor-CLEAN is the fact that no assumptions are made concerning the precise pulse shape and duration of received MPCs. Also, the number of paths does not have to be predefined.

The Sensor-CLEAN has been modified and enhanced in a variety of publications [LKV07].

UWB-SAGE The SAGE algorithm that is also extended for UWB signals in this thesis, has been adapted for parameter estimation in UWB channels before. The so-called UWB-SAGE [HT03b], [HT03a] aims to estimate amplitudes, azimuth angles, elevation angles and delays of MPCs in the frequency domain. The received signal is assumed to be the sum of a predefined number of MPCs of known shape. Furthermore, the UWB channel is expressed as a set of smaller subbands. Within each subband, scattering loss and antenna directivity are assumed to be constant. In one iteration of the UWB-SAGE, the parameters of one single wave are estimated by maximizing a cost function obtained by summation of the cost functions of all subbands. (For details on the SAGE see Chapter 4). Similar to the Sensor-CLEAN, an identified wave is canceled from the data before the search for the next component begins.

Utilization of Orthogonal Correlators While Sensor-CLEAN, UWB-SAGE and the approach in this work all rely on interference cancellation techniques, quite a different approach can be found in [dAUK04]. Orthogonal Hermit wavelets are used as a signal processing tool at the receiver array. The approach exploits the correlation function properties of such wavelets to extract conditions directly from the UWB-IR signal that allow the use of conventional narrowband parameter estimation techniques such as MUSIC [Sch86] or the Capon beamformer [Cap69] to enable delay and angle-of-arrival estimation of MPCs [dAUK04].

Chapter 3

Signal Model

This Chapter explains the underlying signal model used for the estimation procedure. The signal model is based on existing models for parameter estimation using the EM or SAGE algorithm with wideband signals, as can be found in [FW88], [FTH+99], [FDHT96], [FRB97] and [PFM97]. Instead of transmitting a periodically repeated burst signal that consists of a wideband shaping pulse modulated by a sounding sequence, the transmitted signal in this model is a single UWB pulse burst. Due to the large bandwidth, excellent time resolution can be achieved in the estimation procedure to resolve the different waves that impinge at the receiver.

A single input multiple output (SIMO) antenna configuration with one transmitter and a measurement array with M equidistant antennas at the receiver serves as transmission scheme. Both transmitter and receiver are considered to remain approximately stationary for the duration of a measurement, and therefore Doppler spread does not have to be considered in the propagation model.

All the described signals are given in their baseband representations, as the following estimation is performed in the baseband.

The transmitted signal $p(t)$ is a single UWB pulse. It is assumed in the propagation model that the received signal $\underline{Y}(t)$ consists of a finite number L of plane waves that are impinging at the receiver antennas. The received signal at the output of the antenna array can be expressed in vector notation as a superposition of these L multipath components,

corrupted by additive noise as

$$\begin{aligned}\underline{Y}(t) &\triangleq [Y_1(t),\ldots,Y_M(t)]^T \\ &= \sum_{l=1}^{L} \underline{s}(t;\underline{\theta}_l) + \sqrt{\frac{N_0}{2}}\underline{N}(t) \\ &= \underline{s}(t;\underline{\theta}) + \sqrt{\frac{N_0}{2}}\underline{N}(t). \end{aligned} \tag{3.1}$$

In this equation the vector $\underline{N}(t) \triangleq [N_1(t),\ldots,N_M(t)]^T$ contains spatially independent complex white Gaussian noise and N_0 is a positive constant, while $\underline{s}(t;\underline{\theta}_l)$ stands for the contribution of the lth multipath component to the M received baseband signals. All wave contributions are summed up in $\underline{s}(t;\underline{\theta}) \triangleq \sum_{l=1}^{L} \underline{s}(t;\underline{\theta}_l)$, where $\underline{\theta} \triangleq [\underline{\theta}_1,\ldots,\underline{\theta}_L]$ contains the parameters of all the waves.

A single multipath component with index l is characterized by its relative delay τ_l, incident azimuth ϕ_l and complex amplitude α_l. These parameters are contained in the vector $\underline{\theta}_l \triangleq [\tau_l, \phi_l, \alpha_l]$. The vector of the contribution of the lth wave to the M received baseband signals is given by

$$\begin{aligned}\underline{s}(t;\underline{\theta}_l) &\triangleq [s_1(t;\underline{\theta}_l),\ldots,s_M(t;\underline{\theta}_l)]^T \\ &= \underline{c}(\phi_l)\ \alpha_l\ p(t-\tau_l) \end{aligned} \tag{3.2}$$

where $\underline{c}(\phi_l) \triangleq [c_1(\phi_l),\ldots,c_M(\phi_l)]^T$ is the steering vector of the antenna array. Its components are given by

$$c_m(\phi) = f_m(\phi)\ e^{j2\pi\lambda^{-1}(\Delta x_m \cos\phi + \Delta y_m \sin\phi)} \tag{3.3}$$

with λ denoting the wavelength matching the center frequency of the transmitted signal, $f_m(\phi)$ denoting the complex electric field pattern of the mth antenna and Δx_m, and Δy_m standing for the displacement of the mth antenna in x- and y-directions with respect to an arbitrary reference point.

So far, the incident elevation angle ψ has been neglected in the signal model. Since disregarding the elevation angle can cause significant errors in azimuth estimation [FRB97], it is advisable to include elevation in the estimation process, at least for environments where it can be expected that many MPCs will impinge from elevation angles considerably different from 0°. To do so, it is necessary to augment the signal model, or more precisely the steering vector to

$$c_m(\phi,\psi) = f_m(\phi,\psi)\ e^{j2\pi\lambda^{-1}(\Delta x_m \cos\psi\cos\phi + \Delta y_m \cos\psi\sin\phi + \Delta z_m \sin\psi)} \tag{3.4}$$

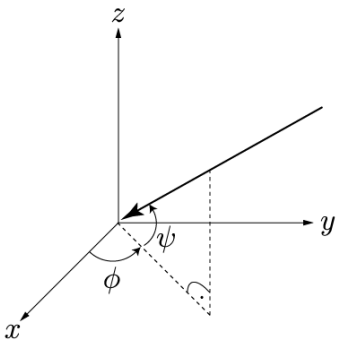

Figure 3.1: Definition of azimuth angle ϕ and elevation angle ψ in three-dimensional Euclidean space.

where Δz_m denotes the antenna displacement in z-direction, so that $\underline{\theta}_l \triangleq [\tau_l, \phi_l, \psi_l, \alpha_l]$ and $\underline{s}(t; \underline{\theta}_l) = \underline{c}(\phi_l, \psi_l)\ \alpha_l\ p(t - \tau_l)$.

For the definition of azimuth and elevation angles in three-dimensional Euclidean space matching this steering vector, see Figure 3.1.

Chapter 4

Parameter Estimation

This Chapter illustrates the SAGE algorithm estimation procedure that is used to obtain the desired wave parameters. First, the reason why it is necessary to use a more elaborate algorithm such as the SAGE algorithm instead of a maximum likelihood estimator is accounted for. Since it is essential for understanding the SAGE algorithm, the method on which the SAGE algorithm is based on, the EM algorithm, is described. Then the SAGE estimation procedure itself is explained, as well as the extension that makes the algorithm suitable for analyzing UWB channels.

As the SAGE algorithm is designed only to estimate the wave parameters, but not the number of multipath components impinging at the receiver, the number of waves L has to be predetermined. The value for L has to be chosen large enough to capture all the dominant waves.

In case the incident elevation angles of the MPCs are not required to be included in the estimation, the parameters ψ_l can simply be set to zero for all the following computations.

4.1 Maximum Likelihood Estimation

The problem to be solved is the estimation of the parameters that characterize the L multipath components that impinge at the receiver. For a maximum likelihood estimation this would mean the maximization of the log-likelihood function of the parameter vector $L(\underline{\theta}; \underline{y}(t))$ given an observation $\underline{Y}(t) = \underline{y}(t)$. The function to be maximized can be found via the probability density function of the received signal vector $pdf(\underline{y}(t); \underline{\theta})$, which is given by [Kay93]

$$pdf(\underline{y}(t); \underline{\theta}) = \frac{1}{\sqrt{(\pi N_0)}} e^{-\frac{1}{N_0}\left(\underline{y}(t) - \underline{s}(t; \underline{\theta})\right)}. \tag{4.1}$$

The log-likelihood function $L(\underline{\theta}; \underline{y}(t))$ is then given by [FTH+99]

$$L(\underline{\theta}; \underline{y}(t)) = \frac{1}{N_0} \left(2 \int_T \Re \left\{ \underline{s}^H(t'; \underline{\theta}) \underline{y}(t') \right\} dt' - \int_T \left\| \underline{s}(t'; \underline{\theta}) \right\|^2 dt' \right) \tag{4.2}$$

where T is the observation span. The parameters can be found by maximizing this function by varying the values of $\underline{\theta}$ so that

$$(\hat{\underline{\theta}})_{ML}(\underline{y}(t)) = \arg \max_{\underline{\theta}} \left\{ L(\underline{\theta}; \underline{y}(t)) \right\}. \tag{4.3}$$

Since $L(\underline{\theta}; \underline{y}(t))$ is a non-linear function, the maximization procedure to compute $(\hat{\underline{\theta}})_{ML}(\underline{y}(t))$ is computationally prohibitive for a large number of multipath components L. The maximum likelihood estimation is a $3L$-dimensional procedure, as the values of the complex amplitudes α_l can be expressed in closed form as a function of the other parameters [FTH+99].

4.2 Expectation Maximization Algorithm

To avoid the complex maximum likelihood estimation procedure, the EM algorithm [DLR77], [Moo96] can be applied to solve the problem at hand. For the EM procedure the measured received signal $\underline{Y}(t)$ is regarded as the incomplete, but observable data, which is a function of the complete, but unobservable data $\underline{X}_l(t)$. The individual multipath components, corrupted by a part of the additive noise, are considered as the complete data:

$$\begin{aligned} \underline{X}_l(t) &\triangleq [X_{l,1}(t), \ldots, X_{l,M}(t)]^T \\ &= \underline{s}(t; \underline{\theta}_l) + \sqrt{\frac{\beta_l N_0}{2}} \underline{N}_l(t) \end{aligned} \tag{4.4}$$

where the nonnegative constants β_l have to be chosen to satisfy $\sum_{l=1}^{L} \beta_l = 1$ in order to form a decomposition of the additive noise vector $\underline{N}(t)$ into L parts. Therefore, the complete data is obtained by adding a part of the additive noise to a corresponding replica of the transmitted pulse form, so that the incomplete data can be expressed as (also see Figure 4.1)

$$\underline{Y}(t) = \sum_{l=1}^{L} \underline{X}_l(t). \tag{4.5}$$

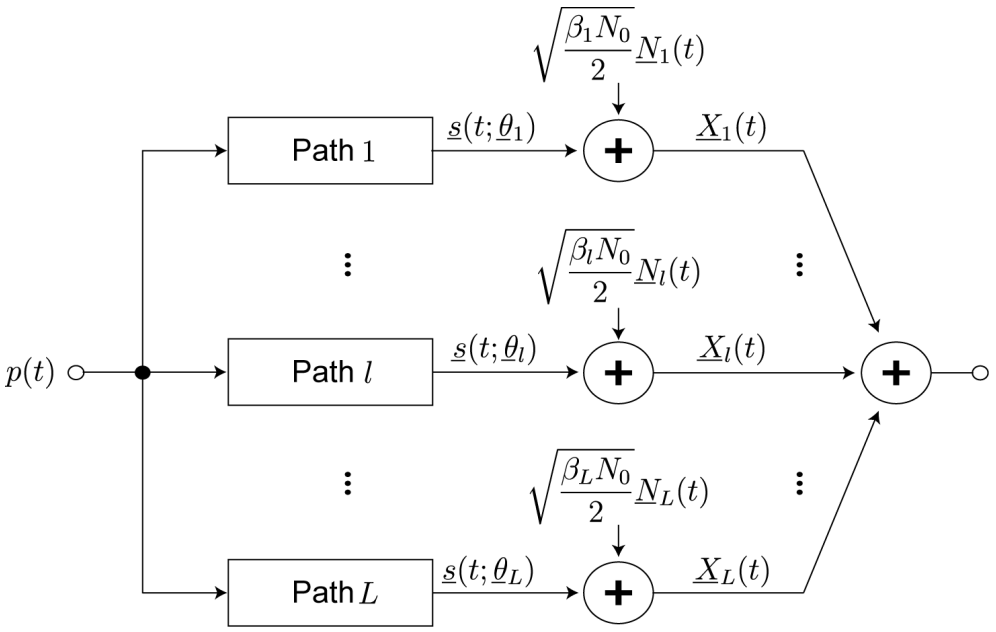

Figure 4.1: Relation between complete and incomplete data [FTH+99].

Similar to (4.2), the log-likelihood function $L(\underline{\theta}_l; \underline{x}_l(t))$ of the parameter vector $\underline{\theta}_l$ of one single wave for an observation $\underline{X}_l(t) = \underline{x}_l(t)$ is given by

$$L(\underline{\theta}_l; \underline{x}_l(t)) = \frac{1}{\beta_l N_0} \left(2 \int_T \Re \left\{ \underline{s}^H(t'; \underline{\theta}_l) \underline{x}_l(t') \right\} dt' - \int_T \left\| \underline{s}(t'; \underline{\theta}_l) \right\|^2 dt' \right) \tag{4.6}$$

and the maximum likelihood estimate of $\underline{\theta}_l$ for an observation $\underline{X}_l(t) = \underline{x}_l(t)$, similar to (4.3), is given by $(\hat{\underline{\theta}}_l)_{ML}(\underline{x}_l(t)) = \arg\max_{\underline{\theta}_l} \{L(\underline{\theta}_l; \underline{x}_l(t))\}$.

Since the complete data is not actually measurable, it has to be estimated from an observation $\underline{Y}(t) = \underline{y}(t)$ of the incomplete data and a previous estimate $\underline{\theta}'$ of the parameter vector by taking its conditional expectation:

$$\hat{\underline{x}}_l(t; \hat{\underline{\theta}}') \triangleq E_{\hat{\underline{\theta}}'} \left\{ \underline{X}_l(t) \mid \underline{y}(t) \right\}. \tag{4.7}$$

This computation is referred to as the Expectation (E) step of the algorithm. Using (4.4) the complete data for a single wave can be computed by [FW88]

$$\hat{\underline{x}}_l(t; \hat{\underline{\theta}}') = \underline{s}(t; \hat{\underline{\theta}}'_l) + \beta_l \left[\underline{y}(t) - \sum_{l'=1}^{L} \underline{s}(t; \hat{\underline{\theta}}'_{l'}) \right]. \tag{4.8}$$

In these equations the first term stands for the contribution of the specific multipath component, and the second term is an estimate of the additive noise, computed by subtracting all wave contributions from the received signal.

The parameter vectors $\underline{\theta}_l$ can then be re-estimated in the so called Maximization (M) step by finding the maximum likelihood estimate

$$\hat{\underline{\theta}}_l'' = (\hat{\underline{\theta}}_l)_{ML}(\underline{\hat{x}}_l(t;\hat{\underline{\theta}}')). \tag{4.9}$$

Furthermore, by inserting (3.2), the M-step for a single multipath component can be divided into two separate steps [PFM97]. In the first step, the maximum likelihood estimates for delay, azimuth and elevation are found by maximizing the absolute value of the cost function $z(\tau,\phi,\psi;\underline{\hat{x}}_l(t;\hat{\underline{\theta}}'))$ via variation of said parameters:

$$\widehat{(\tau_l,\phi_l,\psi_l)}_{ML}(\underline{\hat{x}}_l(t;\hat{\underline{\theta}}')) = \arg\max_{[\tau,\phi,\psi]} \left\{ \left| z(\tau,\phi,\psi;\underline{\hat{x}}_l(t;\hat{\underline{\theta}}')) \right| \right\} \tag{4.10}$$

where

$$z(\tau,\phi,\psi;\underline{\hat{x}}_l(t;\hat{\underline{\theta}}')) \triangleq \int_0^T p^*(t'-\tau)\ \underline{c}^H(\phi,\psi)\ \underline{\hat{x}}_l(t';\hat{\underline{\theta}}')\ dt' \tag{4.11}$$

and $\|\underline{c}(\phi,\psi)\|^2 = \sum_{m=1}^{M} |f_m(\phi,\psi)|^2$, which, considering an approximately uniform antenna pattern for all incident angles, equals M.

The cost function can be realized by performing narrowband beamforming to compensate for the phase differences of the signals arriving at different antennas, and then passing the result of the beamforming procedure through a filter matched to the transmitted pulse form [FW88], [FTH+99].

In the second part of the M-step the complex gain is estimated separately by simply dividing the cost function by the energy of the transmitted pulse weighted by the antenna gain for the previously estimated angles [FDHT96]:

$$(\hat{\alpha})_{ML}(\underline{\hat{x}}_l(t;\hat{\underline{\theta}}')) = \frac{z(\widehat{(\tau_l,\phi_l,\psi_l)}_{ML}(\underline{\hat{x}}_l(t;\hat{\underline{\theta}}'));\underline{\hat{x}}_l(t;\hat{\underline{\theta}}'))}{\left\|\underline{c}((\hat{\phi}_l,\hat{\psi}_l)_{ML}(\underline{\hat{x}}_l(t;\hat{\underline{\theta}}')))\right\|^2 \int_0^T \left| p(t'-(\hat{\tau}_l)_{ML}(\underline{\hat{x}}_l(t';\hat{\underline{\theta}}'))) \right|^2 dt'}. \tag{4.12}$$

E-step and M-step are consecutively executed, generating a sequence of estimates $\{\hat{\underline{\theta}}(\mu)\}$, $\mu = 0,1,\ldots$, until convergence is achieved. Even though guaranteed to converge under certain mild conditions, the EM algorithm does not necessarily converge to a global maximum [Kay93]. Another property of the EM algorithm is that for any generated sequence $\{\underline{\theta}(\mu)\}$, the sequence of log-likelihood values $\{L(\hat{\underline{\theta}}(\mu);\underline{y}(t))\}$ doesn't decrease [FTH+99], [DLR77].

As shown in the signal flow graph in Figure 4.2, the EM algorithm reduces the complexity to L 3-dimensional estimation procedures, which can be performed simultaneously.

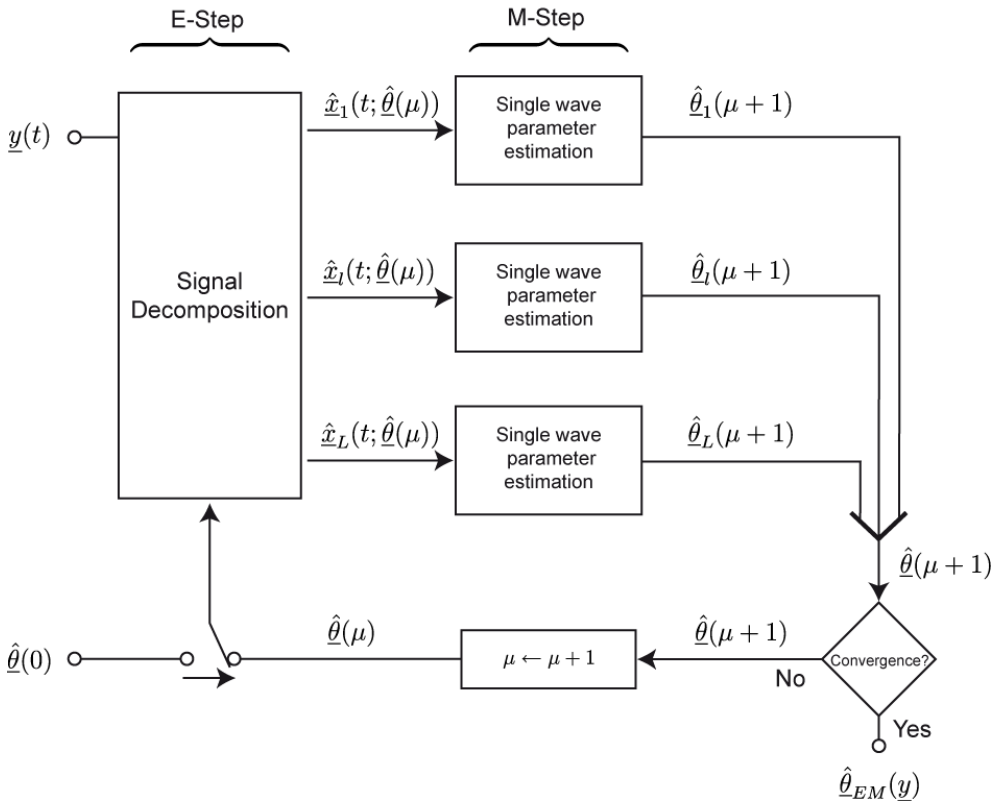

Figure 4.2: Signal flow graph of the EM algorithm [FTH+99].

4.3 Space-Alternating Generalized Expectation Maximization Algorithm

The SAGE algorithm is an extension of the EM algorithm. Each iteration of the SAGE algorithm is an EM iteration, but instead of updating all parameters at once, only subsets of parameters are estimated in on iteration step. This means that rather than using one complete data space, parameters are separated into smaller groups associated with smaller data spaces, which can be considered complete if the other parameters are known. The parameter groups are then updated sequentially. This leads to faster convergence rates and simplifies the maximization process [FH94].

For the estimation problem examined in this thesis, the parameter vector $\underline{\theta}$ is split into L subsets $\underline{\theta}_l$ with their complete data spaces $\underline{X}_l(t)$. Thus, in one iteration step of the SAGE algorithm the parameters of one multipath component are re-estimated (see Figure 4.3). For the re-estimation of all L wave parameters it takes one SAGE cycle, consisting of L iteration steps. The SAGE algorithm and the EM algorithm are of identical computational complexity.

Since less informative complete data spaces improve the asymptotic convergence rate of the algorithm [FH94], β_l is selected to equal 1, as this setting minimizes the information provided by $\underline{X}_l(t)$ about $\underline{\theta}_l$ [PFM97].

The complexity of the SAGE procedure can be reduced by replacing the 3-dimensional estimation procedure with three 1-dimensional procedures. To achieve this, the parameter subsets can be divided into even smaller subsets, so that the parameters can be estimated individually. The updated parameters $\hat{\tau}_l''$, $\hat{\phi}_l''$, and $\hat{\psi}_l''$ are obtained by successively varying only one parameter, while keeping the other parameters fixed to their previously estimated value. Parameters marked by (.′) originate from a prior SAGE cycle, whereas (.″) indicates an estimate from the current cycle. The update α_l'' is computed by inserting the freshly estimated parameters in (4.12) [FTH+99]:

$$\begin{aligned}
\hat{\tau}_l'' &= \arg\max_{\tau} \left\{ \left| z(\tau, \hat{\phi}_l', \hat{\psi}_l'; \underline{\hat{x}}_l(t; \hat{\underline{\theta}}')) \right| \right\} \\
\hat{\phi}_l'' &= \arg\max_{\phi} \left\{ \left| z(\hat{\tau}_l'', \phi, \hat{\psi}_l'; \underline{\hat{x}}_l(t; \hat{\underline{\theta}}')) \right| \right\} \\
\hat{\psi}_l'' &= \arg\max_{\psi} \left\{ \left| z(\hat{\tau}_l'', \hat{\phi}_l'', \psi; \underline{\hat{x}}_l(t; \hat{\underline{\theta}}')) \right| \right\} \\
\hat{\alpha}_l'' &= \frac{z(\hat{\tau}_l'', \hat{\phi}_l'', \hat{\psi}_l''; \underline{\hat{x}}_l(t; \hat{\underline{\theta}}'))}{\left\| \underline{c}(\hat{\phi}_l'', \hat{\psi}_l'') \right\|^2 \int_0^T |p(t' - \hat{\tau}_l'')|^2 \, dt'}.
\end{aligned} \tag{4.13}$$

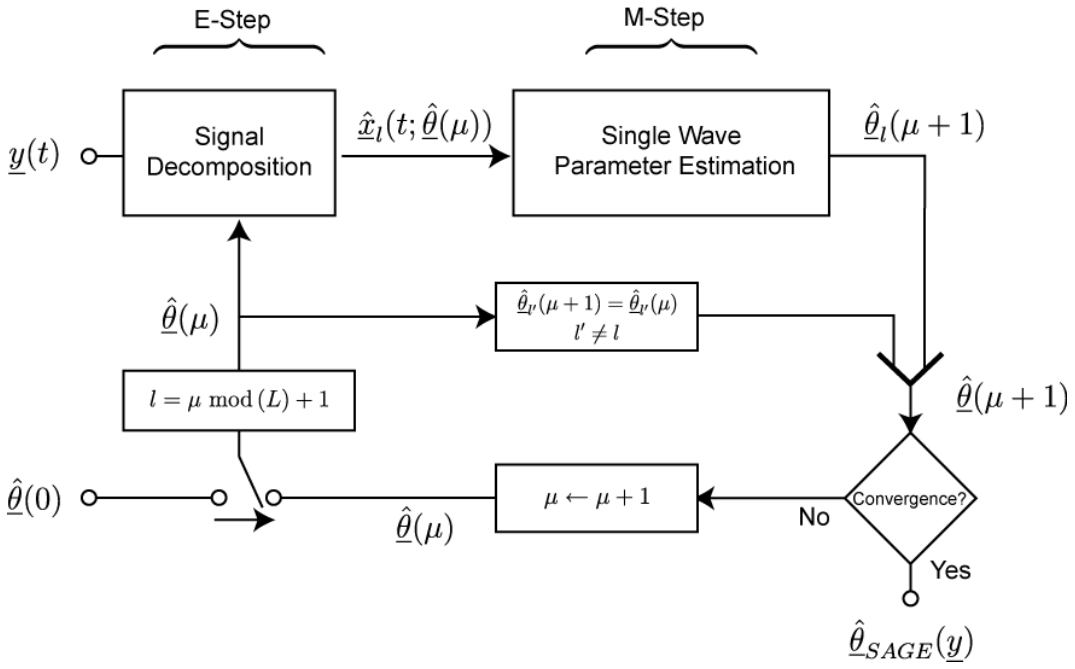

Figure 4.3: Signal flow graph of the SAGE algorithm [FTH+99].

4.3.1 Initialization of the SAGE Algorithm

Successive interference cancellation is used to compute an initial estimate $\underline{\theta}(0)$ of the parameters [FTH+99]. Similar to one SAGE cycle, the initialization takes L steps, one per wave. Starting with all parameters set to zero, the initial parameter values for the lth multipath component are computed by

$$\begin{aligned}
\hat{\tau}_l(0) &= \arg\max_{\tau} \left\{ \sum_{m=1}^{M} \left| \int_0^T p^*(t'-\tau)\, \hat{x}_{l,m}(t';\hat{\underline{\theta}}')dt' \right|^2 \right\} \\
\hat{\phi}_l(0) &= \arg\max_{\phi} \left\{ \left| \int_0^T p^*(t'-\hat{\tau}_l(0))\, \underline{c}^H(\phi,0)\, \underline{\hat{x}}_l(t';\hat{\underline{\theta}}')dt' \right|^2 \right\} \\
\hat{\psi}_l(0) &= \arg\max_{\psi} \left\{ \left| \int_0^T p^*(t'-\hat{\tau}_l(0))\, \underline{c}^H(\hat{\phi}_l(0),\psi)\, \underline{\hat{x}}_l(t';\hat{\underline{\theta}}')dt' \right|^2 \right\} \\
\hat{\alpha}_l(0) &= \frac{z(\hat{\tau}_l(0),\hat{\phi}_l(0),\hat{\psi}_l(0);\underline{\hat{x}}_l(t;\hat{\underline{\theta}}'))}{\left\| \underline{c}(\hat{\phi}_l(0),\hat{\psi}_l(0)) \right\|^2 \int_0^T |p(t'-\hat{\tau}_l(0))|^2\, dt'}
\end{aligned} \tag{4.14}$$

with

$$\begin{aligned}
\underline{\hat{x}}_l(t;\hat{\underline{\theta}}') &= \underline{y}(t) - \sum_{l'=1}^{l-1} \underline{s}(t;\underline{\theta}_{l'}) \\
\underline{\hat{x}}_1(t;\hat{\underline{\theta}}') &= \underline{y}(t).
\end{aligned} \tag{4.15}$$

4.4 SAGE for UWB

Since the UWB sounding pulse provides extremely high time resolution, applying narrowband beamforming can lead to multiple detection of strong waves and because of that, the unmodified SAGE algorithm is not an optimal solution for the problem. The reason for multiple wave detections is that only the differences in the phases of the MPCs arriving at different antenna locations are considered, but not the slight differences in time. For a narrowband signal with low time resolution this would not cause any problem, but for an UWB signal, the time differences at the antennas can be resolved. Therefore, when correcting the phase differences and then adding up the signals from the M antennas, as done in the beamforming part, more than one maximum for one and the same wave might occur. These maxima can then lead to the repeated detection of that specific wave. An illustration of this problem is shown in Figure 4.4.

The highest peaks of the signals $Y_1(t)$ and $Y_2(t)$ respectively, measured for a transmitted pulse with 4000MHz bandwidth at center frequency 5500MHz, is the line-of-sight (LOS) MPC. It arrives with about 0.8ns time difference from an azimuth angle of 120° at the two different antennas, which are spaced by about 25.5cm at 45°. After beamforming for the LOS angles, it is clearly visible that more than one maximum arises, which would lead to multiple LOS detections.

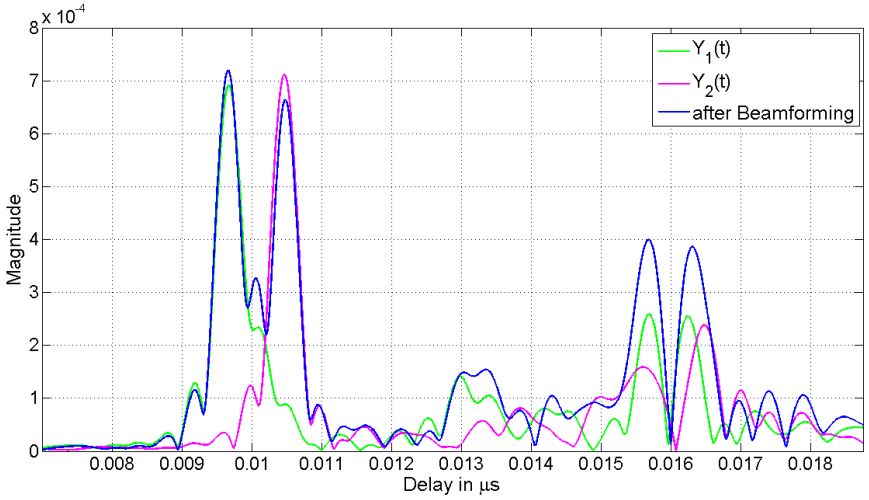

Figure 4.4: Illustration of multiple detection problem.

A possible way to avoid multiple MPC detections is to exclude short time intervals around the delays of already detected waves from the estimation process of other waves. For the span of the time intervals, the possible time differences of a wave arriving at different antenna locations should be considered. Hence, the time intervals depend on the spatial extent of the antenna array. The easiest way to define the time intervals is to simply compute the largest possible time-of-flight between any two antennas of the array. The time interval $\tau_{e,l}$ around the lth MPC, which is excluded from estimation for all other MPCs with $l' \neq l$, is given by

$$\tau_{e,l} = \left[\tau_l - \frac{d_{max}}{c},\ \tau_l + \frac{d_{max}}{c}\right] \tag{4.16}$$

where d_{max} is the largest distance between two antennas of the measurement array and c is the speed of light, so that

$$\widehat{(\tau_l, \phi_l, \psi_l)}_{ML}(\hat{\underline{x}}_l(t;\hat{\underline{\theta}}')) = \arg \max_{[\tau,\phi,\psi]} \left\{ \left| z(\tau,\phi,\psi;\hat{\underline{x}}_l(t;\hat{\underline{\theta}}')) \right| \right\} \Big|_{\tau \notin \tau_{e,l'}\ \forall\, l' \neq l}. \tag{4.17}$$

The time restriction only affects the estimation of the delay parameter in (4.13) and (4.14). Those equations change to

$$\hat{\tau}_l'' = \arg\max_{\tau} \left\{ \left| z(\tau, \hat{\phi}_l', \hat{\psi}_l'; \underline{\hat{x}}_l(t; \underline{\hat{\theta}}')) \right| \right\} \Big|_{\tau \notin \tau_{e,l'} \; \forall \, l' \neq l} \tag{4.18}$$

and

$$\hat{\tau}_l(0) = \arg\max_{\tau} \left\{ \sum_{m=1}^{M} \left| \int_0^T p^*(t' - \tau) \; \hat{x}_{l,m}(t'; \underline{\hat{\theta}}') dt' \right|^2 \right\} \Big|_{\tau \notin \tau_{e,l'} \; \forall \, l' \neq l} . \tag{4.19}$$

Time gating lowers the temporal resolution. Since the time restriction intervals increase with antenna array size, this fact has to be kept in mind when choosing an appropriate array.

Chapter 5

Results

For the presentation of the results obtained by the application of the SAGE algorithm, several UWB measurements are examined to demonstrate the capabilities and weaknesses of the algorithm in different environments. The measurements were all taken with vector network analyzers and UWB pulse transmission then has been simulated with a raised-cosine pulse shape. The environments in which the measurements took place vary in size as well as the amount of inventory, and therefore display distinct reflection and scattering characteristics.

In order to evaluate the performance of the algorithm, various settings are applied. Each environment is analyzed for different antenna array configurations. All the array configurations have in common that the spacing between the antennas always is half the wavelength of the upper frequency band-edge to avoid ambiguities of the directions-of-arrival at all frequencies [Mol09]. Furthermore, as the definition of UWB includes a wide range of possible bandwidths, the algorithm is applied for pulse transmission with different bandwidths.

5.1 Measurement Analysis 1

In this Section, measurement data that was taken by IMST GmbH within the "why-less.com" project is analyzed [IMS], [why]. The measuring system was set up in an office of about 5mx5m in size and 2.75m in height. As there was only very little inventory in the office and receiver and transmitter antennas were positioned at the same height, the elevation angles of the received waves are expected to be mainly close to 0°. In addition to that, the measurements were taken in the x-y-plane only, and therefore elevation is neglected in the estimation process. It is assumed that the antenna used for the measurements is

omnidirectional, meaning $f_m(\phi, \psi) = 1$ for $m = 1, \ldots, M$.

Two scenarios are analyzed. In one of them, an LOS connection between transmitter and receiver exists, in the second the direct path is obstructed by a metal cabinet (see Figure 5.1). In each scenario the transmitter antenna was placed in a fixed position at 1.5m height, and the receiver antenna was moved along 30 parallel tracks spaced by 1cm in 150 steps of 1cm at 1.5m height in the x-y-plane.

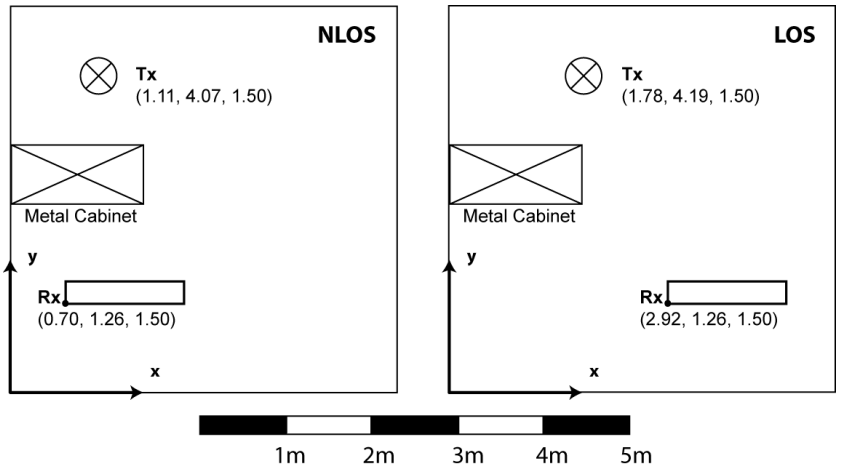

Figure 5.1: Measurement setup LOS and NLOS scenario [IMS].

For the demonstration of the results, UWB pulse transmission is simulated for different antenna array configurations at several positions in the available measurement grid. Spacing between the antennas is chosen to be 2cm, so that the upper frequency band-edge of the transmitted pulse has to be 7500MHz.

5.1.1 LOS Scenario

For the illustration of the estimated delays and azimuths of the MPCs, the detected paths are plotted across the azimuth-delay scattering function for an elevation of 0°, arising from the associated measurement array. This function represents the average received power as a function of azimuth and delay. It can be computed with the help of the steering vector by [PNG08]

$$S(\tau, \phi) = \left| \sum_{m=1}^{M} Y_m(\tau) e^{-j2\pi\lambda^{-1}(\Delta x_m \cos\phi + \Delta y_m \sin\phi)} \right|^2 . \tag{5.1}$$

In Figures 5.2–5.5 the results of the proposed estimation procedure are shown for the LOS scenario for a 10x10 rectangular antenna array, positioned on the left edge of the measurement grid, for different bandwidths. From previous measurement analyses in [KP03b],

[KP03a], [KP02] and [why] the number of paths L can be expected to be rather small, and therefore is set to 10. Detected MPCs are plotted in greyscales according to their energy. The darker the dots, the stronger the energy of the wave. To demonstrate again why the introduction of the time restriction intervals is imperative, the result of the unmodified SAGE algorithm for 4000MHz bandwidth is shown in Figure 5.6. When comparing this plot to the 4000MHz plot of the proposed algorithm, it is obvious that without time gating the strong LOS MPC is detected multiple times and that the algorithm fails to detect other strong waves.

Comparing the results of the modified algorithm for different bandwidths, it can be observed that with the lowest time resolution of 500MHz bandwidth, none of the MPCs is detected more than once. For higher time resolutions, despite the introduced time restriction intervals, the LOS component and other strong waves are still detected more than once, though with little energy. On the other hand, at low time resolution MPCs are detected that at higher resolutions don't seem to actually be deterministic waves, as can also be seen in the azimuth-delay scattering function. Both these problems could be solved by choosing a more adequate number of paths L, though without exact knowledge of the number of received signal paths this could lead to undetected MPCs.

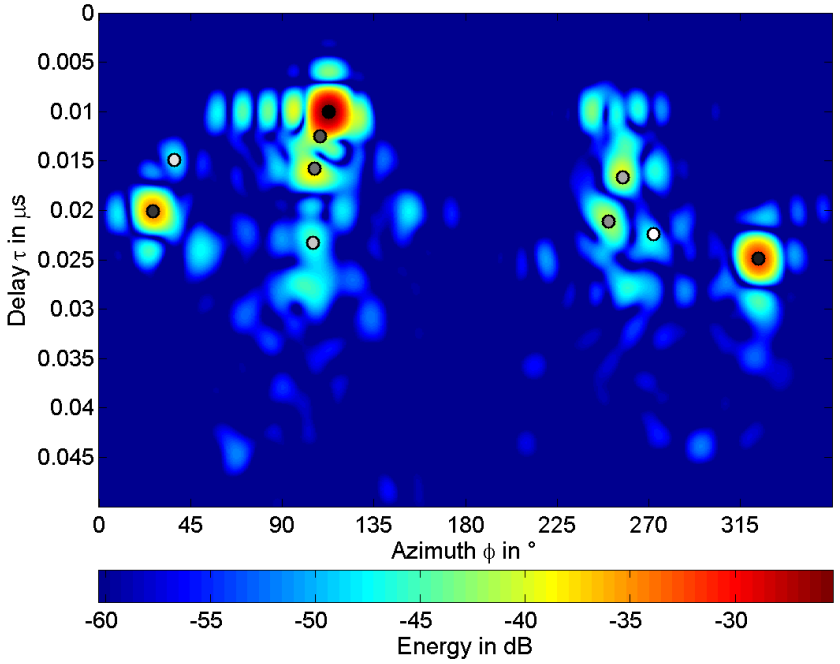

Figure 5.2: Result for 10x10 antenna array, B = 500MHz.

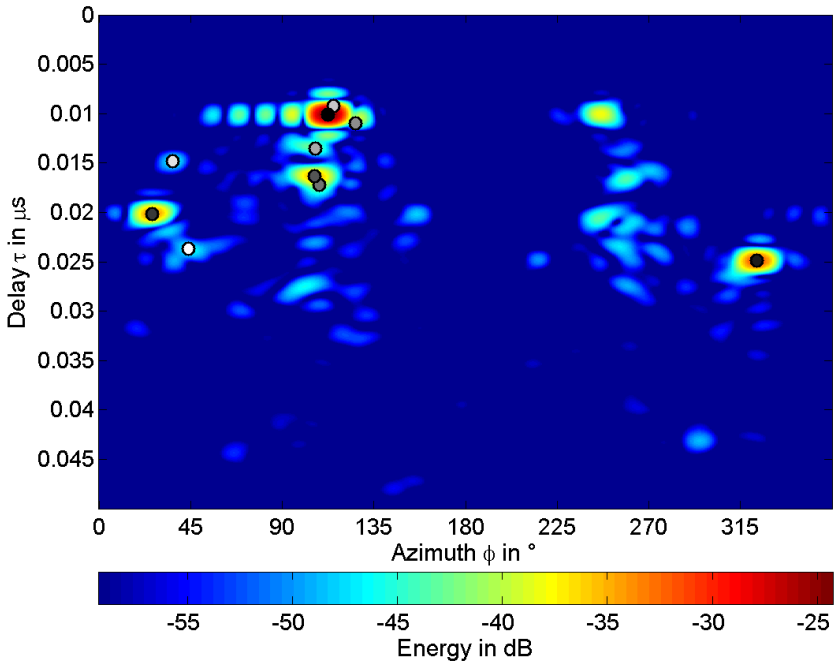

Figure 5.3: Result for 10x10 antenna array, B = 1000MHz.

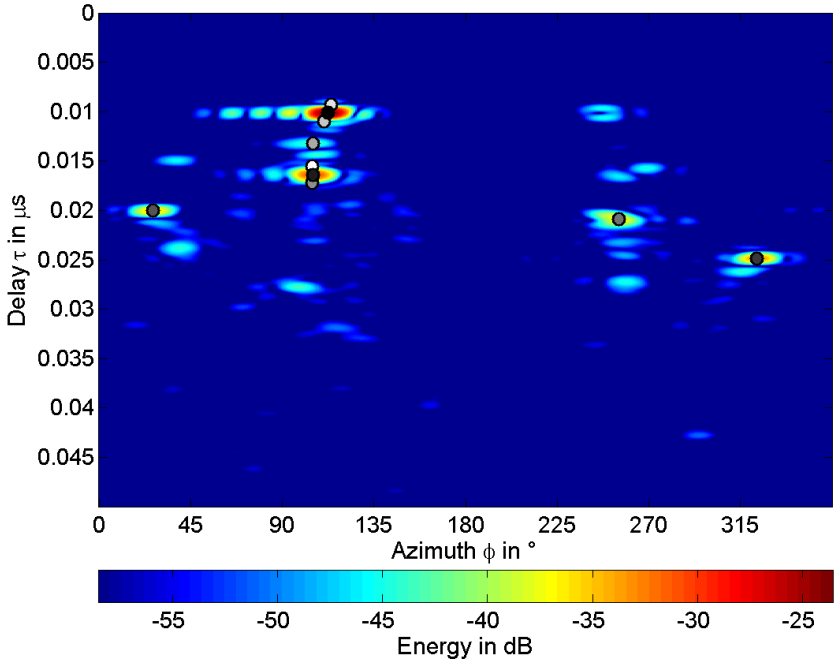

Figure 5.4: Result for 10x10 antenna array, B = 2000MHz.

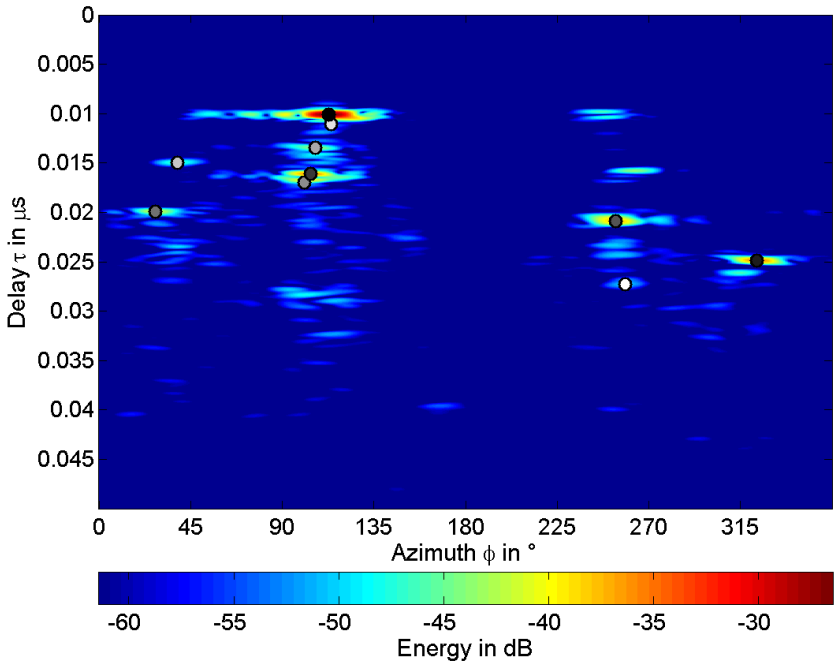

Figure 5.5: Result for 10x10 antenna array, B = 4000MHz.

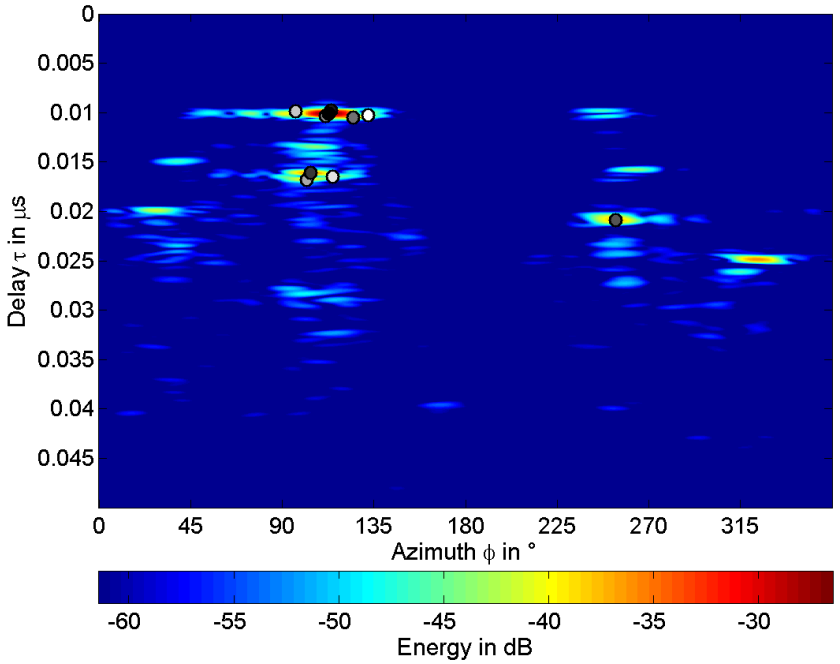

Figure 5.6: Result of unmodified SAGE for 10x10, B = 4000MHz.

The five strongest MPCs that are detected with each of the four bandwidths are the LOS wave from about 120° impinging at 10ns, followed by two waves from approximately the same direction that are probably reflections from floor and ceiling at 13ns and 16ns. A reflection from the wall to the right reaches the receiver at 20ns from 35°, and a MPC originating from a reflection behind the array impinges at 25ns from 325°. An interpretation of these results is illustrated in Figure 5.7.

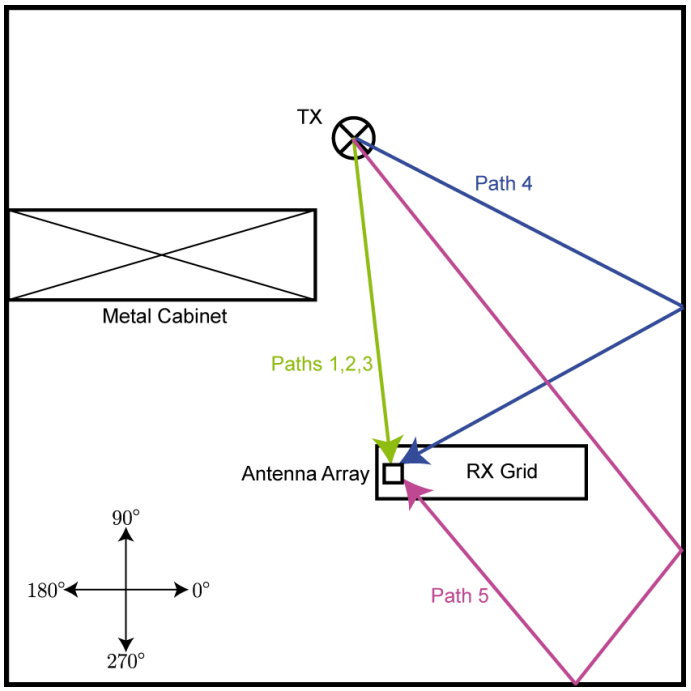

Figure 5.7: Strongest detected waves.

To visualize the influence of the antenna array size, the SAGE algorithm is applied for rectangular receiver arrays with 10x2, 10x3 and 10x10 antennas. Figures 5.5–5.9 show the results for a 4000MHz bandwidth. The azimuth estimation benefits from the use of more antennas, as can be seen when comparing the results for the MPC arriving at 20ns from 35°. Nevertheless, the use of only two lines of ten antennas each provides enough information to resolve angles mirrored along the x-axis.

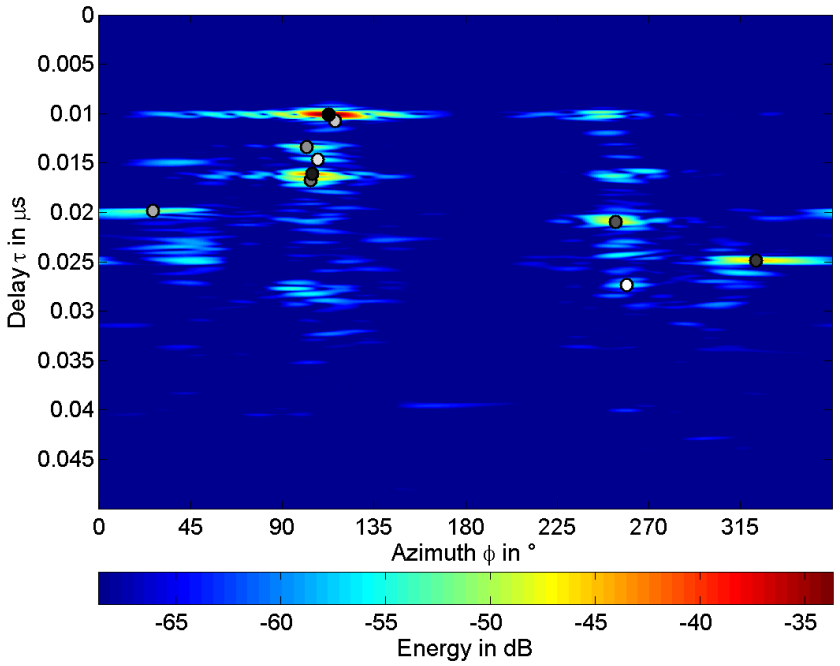

Figure 5.8: Result for 10x3 antenna array, B = 4000MHz.

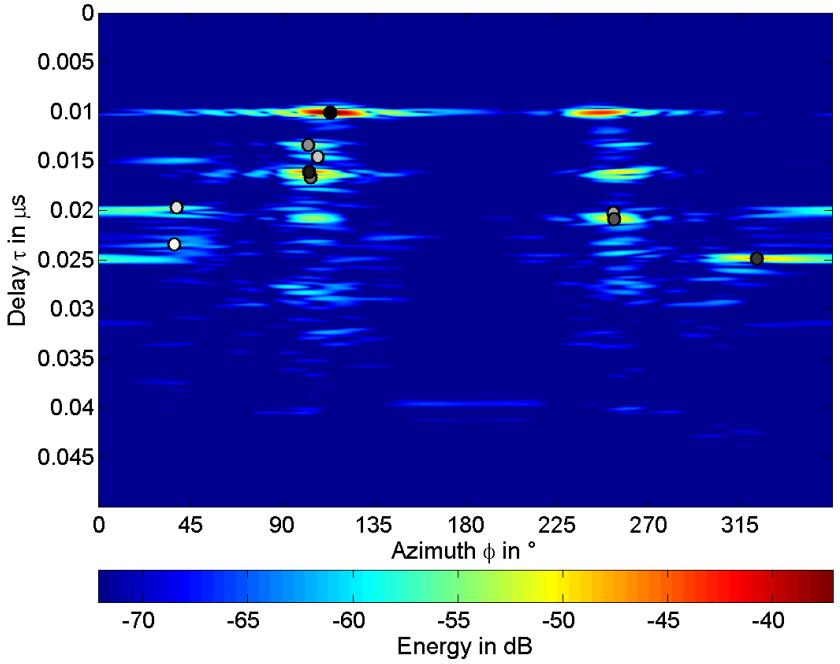

Figure 5.9: Result for 10x2 antenna array, B = 4000MHz.

Taking a look at the average energy within an array captured in the estimation procedure compared to the average received energy in Table 5.1, it becomes obvious that the percentage of the estimated energy decreases with bandwidth and array size. This results from the higher time resolution at larger bandwidths, which causes the received energy to disperse into more delay bins. Therefore, the probability that the captured energy originates from deterministic MPCs only, is higher than at lower time resolutions. In addition to that, the time restriction interval that was introduced to avoid multiple wave detection prevents the capturing of all the energy originating from one wave at different antennas within the time interval. As the time interval increases with array size, the captured energy decreases with array size. Furthermore, with increasing bandwidth, MPCs become increasingly distorted. Since this can cause one MPC to disperse into more delay bins than the original pulse shape, not all the energy of a MPC can be captured.

Bandwidth	10x2 Array	10x3 Array	10x10 Array
500MHz	85,39%	83,63%	77,96%
1000MHz	83,34%	82,44%	76,09%
2000MHz	77,27%	76,30%	65,95%
4000MHz	54,50%	52,94%	33,98%

Table 5.1: Average energy captured by estimation in percent of average received energy.

To demonstrate the estimated complex amplitudes, the received signals for a specific antenna within the 10x10 array are reconstructed with (3.2) and compared to the actually received signals (Figures 5.10–5.13). Although the reconstructed signals are not completely accurate, for bandwidths 500MHz, 1000MHz, and 2000MHz, the received signals can be approximated very well. With 4000MHz bandwidth the first impression seems to be that the reconstructed signal does not fit the received signal at all. As a matter of fact, this does not automatically mean that the SAGE algorithm failed to detect MPCs. The peaks in the received signal that do not appear in the estimated one, are probably no deterministic waves at all. Due to the high time resolution, stochastic components are also resolved better than at smaller bandwidths. The algorithm is designed to estimate deterministic MPCs, and therefore the stochastic components are missing in the reconstructed signal.

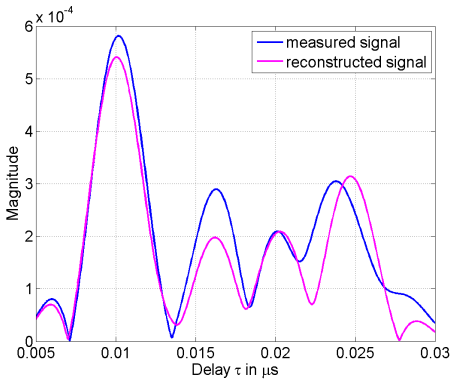

(a) Magnitude representation.

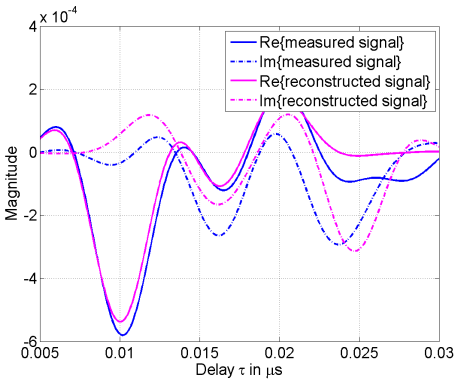

(b) Real/Imaginary part representation.

Figure 5.10: Received and reconstructed signal for B = 500MHz.

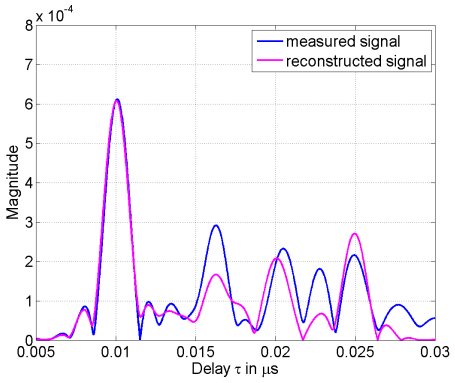

(a) Magnitude representation.

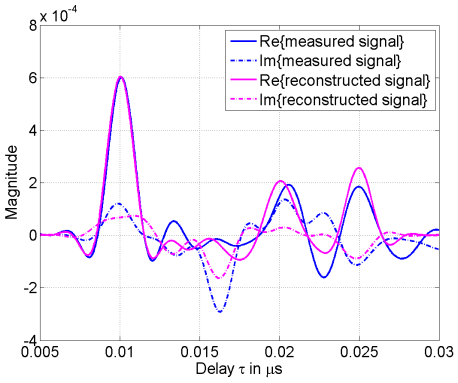

(b) Real/Imaginary part representation.

Figure 5.11: Received and reconstructed signal for B = 1000MHz.

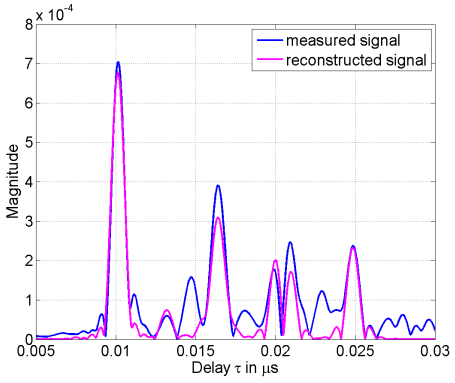

(a) Magnitude representation.

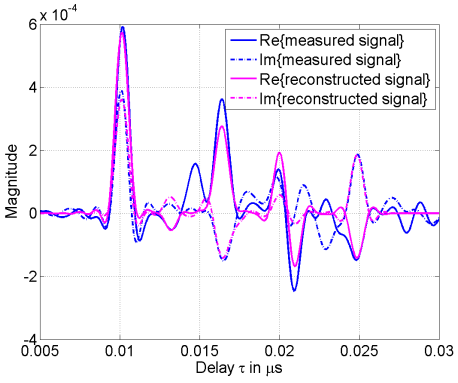

(b) Real/Imaginary part representation.

Figure 5.12: Received and reconstructed signal for B = 2000MHz.

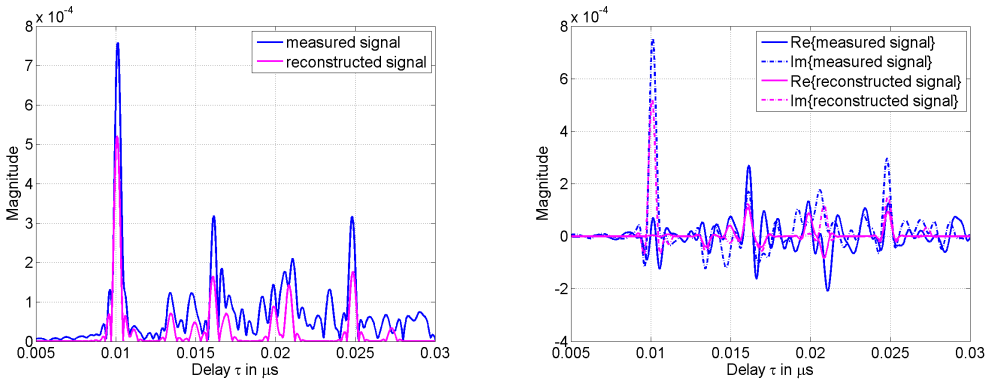

(a) Magnitude representation. (b) Real/Imaginary part representation.

Figure 5.13: Received and reconstructed signal for B = 4000MHz.

Since path tracking possibilities of the obtained results are of interest, these are investigated in Figures 5.14–5.17. For that purpose, propagation of the detected paths through the whole available measurement grid is visualized in Figures 5.14a–5.17a. The Figures show the magnitude of reconstructed signals for estimation with a 10x10 array versus delay, for antennas positioned side by side in a line parallel to the x-axis. Comparing these plots to the magnitude-delay profiles of the measured signals at the same antennas in 5.14b–5.17b, it can be seen that especially for large bandwidths the MPCs can easily be tracked throughout the grid visually .

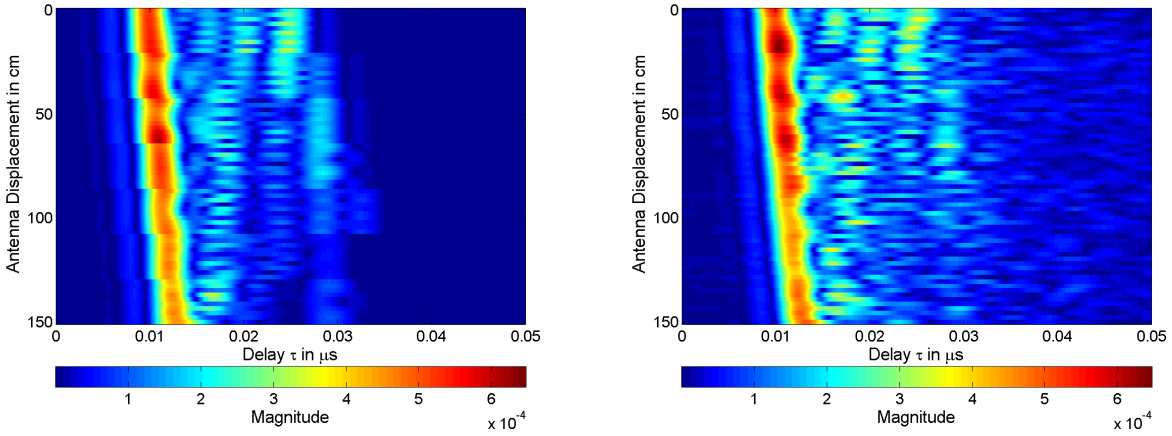

(a) Reconstructed signals. (b) Received signals.

Figure 5.14: Propagation of waves through measurement grid for B = 500MHz.

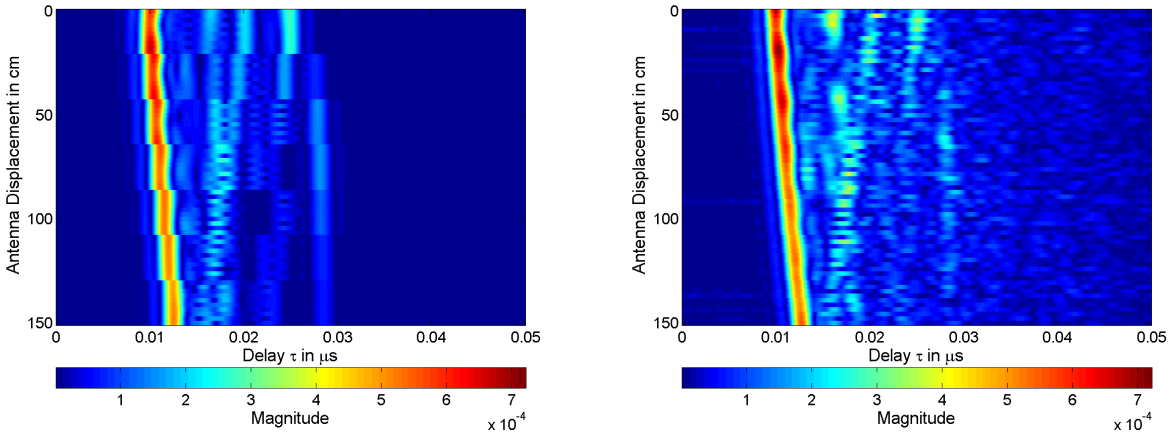

(a) Reconstructed signals. (b) Received signals.

Figure 5.15: Propagation of waves through measurement grid for B = 1000MHz.

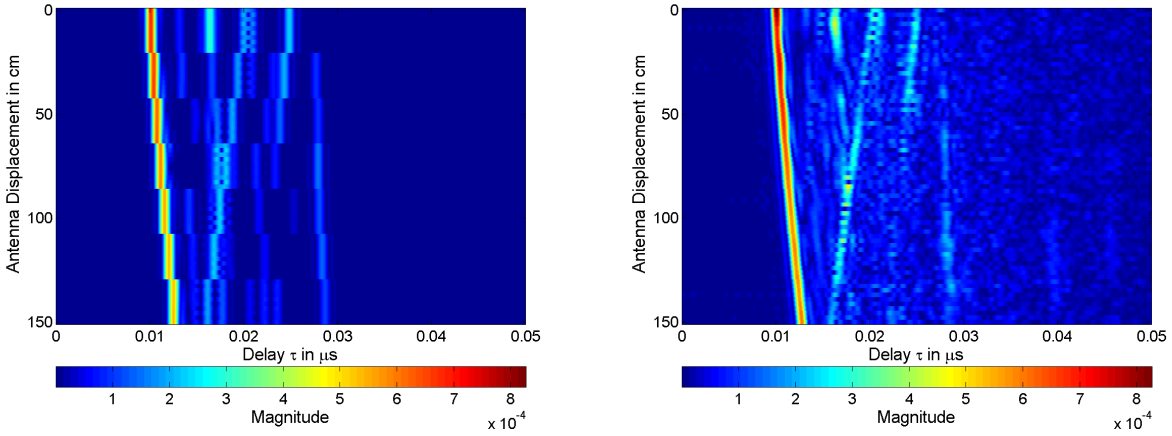

(a) Reconstructed signals. (b) Received signals.

Figure 5.16: Propagation of waves through measurement grid for B = 2000MHz.

The plots also clearly demonstrate the fact that the time difference it takes the waves to reach the different antennas within an array is not considered in the signal model. This negligence causes the propagation path of a wave to show discontinuities at the crossover between two antenna arrays. These discontinuities are not present in the plots for the measured signals. Again, the plots in Figures 5.14–5.17 clarify, why the energy captured at high time resolutions is less than for lower time resolutions, by comparing the noise level between the obvious MPC paths in the plots for the measured signals to the completely energy free spaces between the paths in the plots for the reconstructed signals.

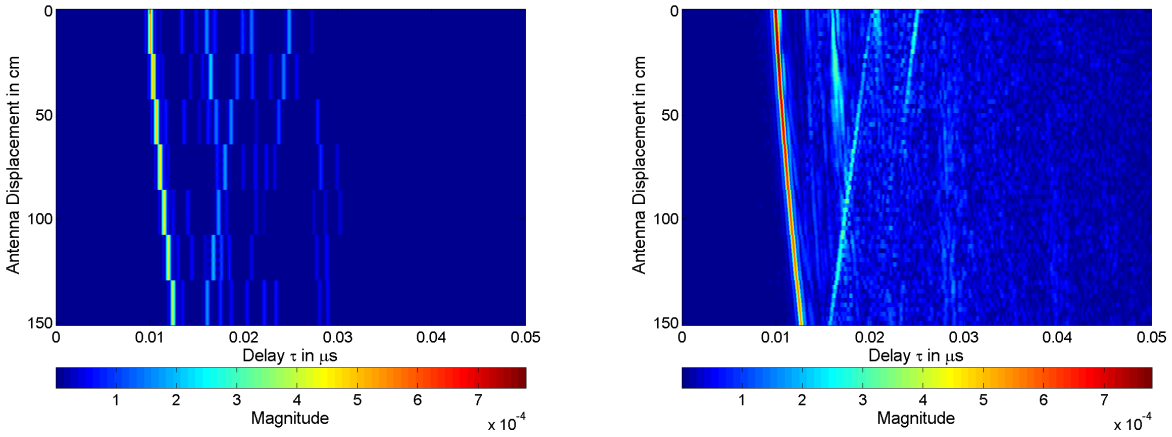

(a) Reconstructed signals.

(b) Received signals.

Figure 5.17: Propagation of waves through measurement grid for B = 4000MHz.

Concerning convergence, no definite conclusions can be drawn. Considering the convergence rates for the LOS wave, it seems that in general faster convergence rates are achieved at larger bandwidths, with exception of the 3x10 array at 1000MHz. This again could be explained by the finer time resolution. Figures 5.18–5.20 show the root mean square errors (RMSEs) of the estimated parameters with respect to the final result of the particular parameter for different array sizes and bandwidths. While for bandwidths 2000MHz and 4000MHz it takes less than 10 SAGE iteration cycles to achieve convergence for all parameters, at 500MHz and 1000MHz it takes less than 20 cycles, except for the 10x3 array at 1000MHz where full convergence is not achieved until 40 cycles.

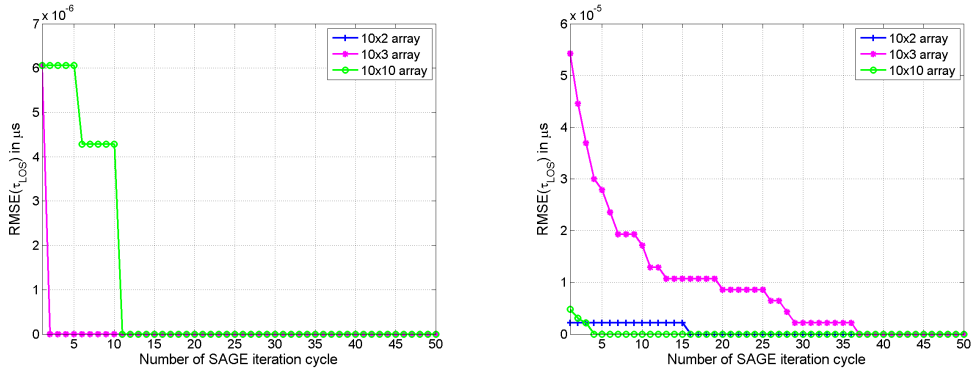

(a) B = 500MHz

(b) B = 1000MHz

Figure 5.18: RMSEs of delay τ for the LOS MPC for 10x2 array, 10x3 array and 10x10 array.

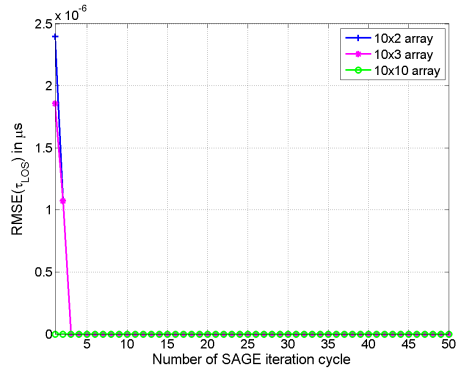

(c) B = 2000MHz

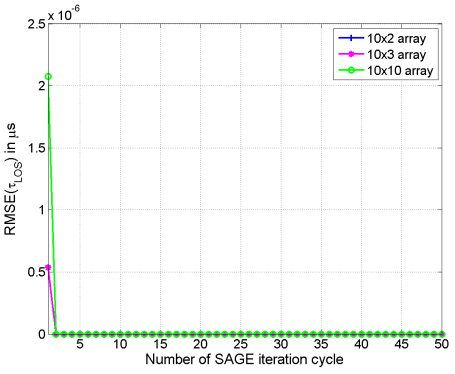

(d) B = 4000MHz

Figure 5.18: RMSEs of delay τ for the LOS MPC for 10x2 array, 10x3 array and 10x10 array.

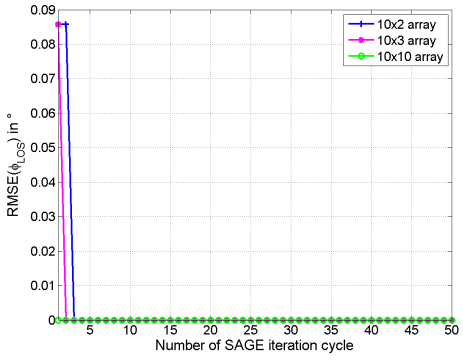

(e) B = 500MHz

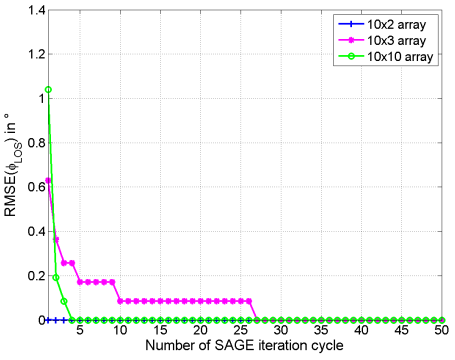

(f) B = 1000MHz

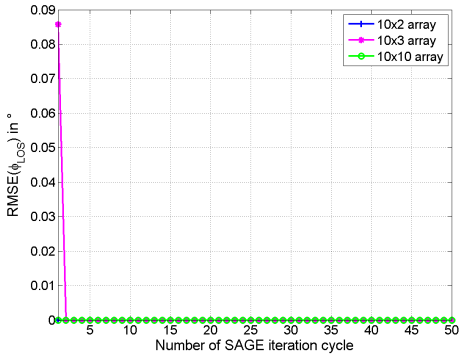

(g) B = 2000MHz

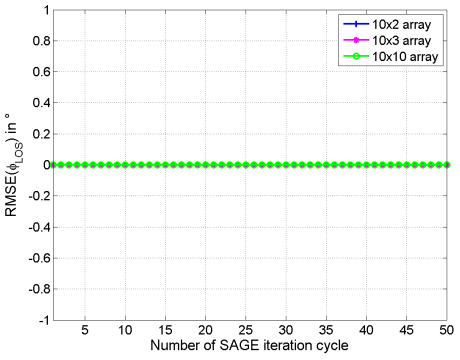

(h) B = 4000MHz

Figure 5.19: RMSEs of azimuth ϕ for the LOS MPC for 10x2 array, 10x3 array and 10x10 array.

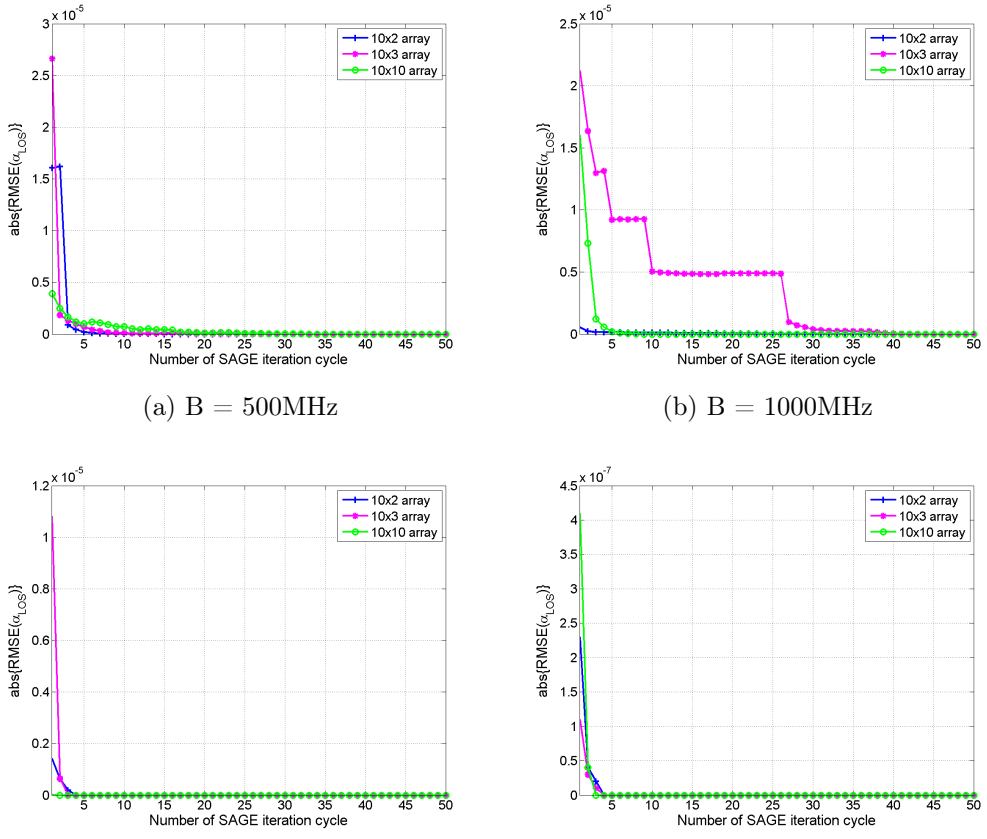

(a) B = 500MHz

(b) B = 1000MHz

(c) B = 2000MHz

(d) B = 4000MHz

Figure 5.20: Absolute value of RMSEs of complex amplitudes α for the LOS MPC for 10x2 array, 10x3 array and 10x10 array.

5.1.2 NLOS Scenario

In this Subsection the NLOS scenario is analyzed. It is known from previous measurement analyses that in this scenario the received signals exhibit a more dense power-delay profile and that a large amount of the received energy results from diffuse scattering rather than deterministic MPCs, as is illustrated in the magnitude-delay profiles for adjoining antenna positions along the x-axis for a 4000MHz bandwidth in Figure 5.21. This, of course, makes it harder to extract the desired channel parameters. In addition to that, the received waves are expected to be temporally close to each other. Since time gating lowers the temporal resolution significantly for large antenna arrays, a 10x10 array is not the best choice for parameter estimation in this case (see Figure 5.35). Therefore, the results presented in Figures 5.22–5.25 arise from a 10x3 antenna array positioned in the middle of the measurement grid. The number of paths is set to 10.

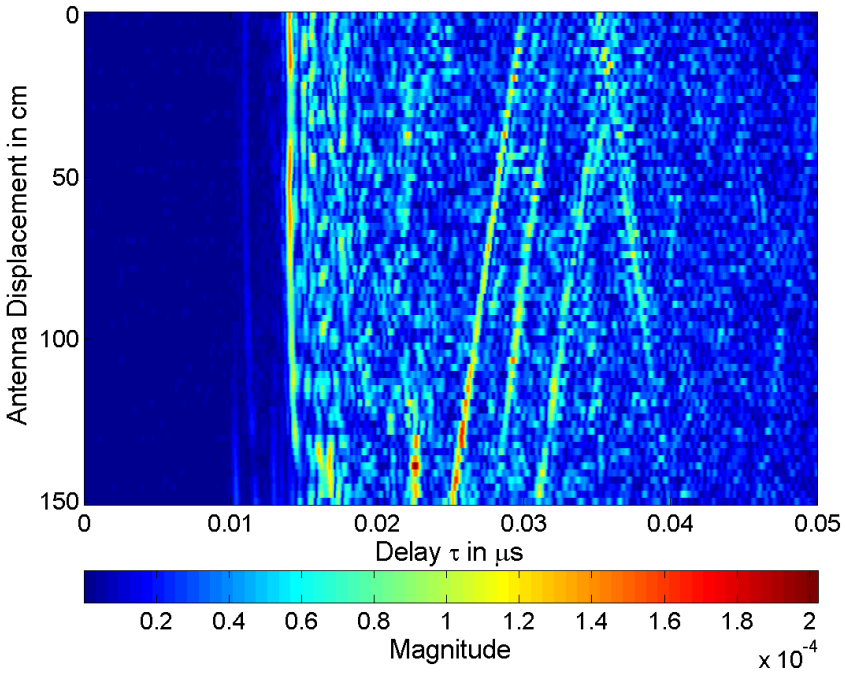

Figure 5.21: Magnitude-delay profiles, B = 4000MHz.

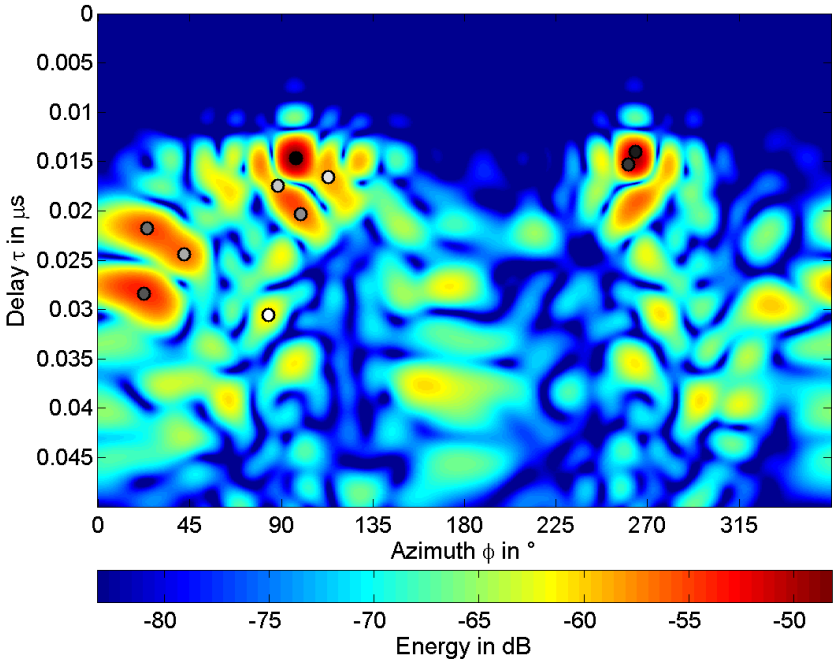

Figure 5.22: Result for 10x3 antenna array, B = 500MHz.

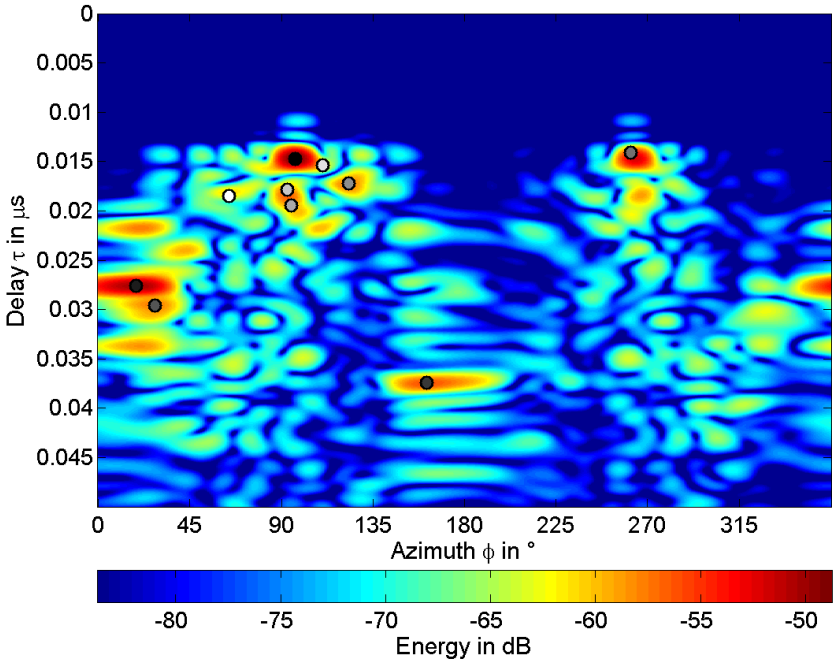

Figure 5.23: Result for 10x3 antenna array, B = 1000MHz.

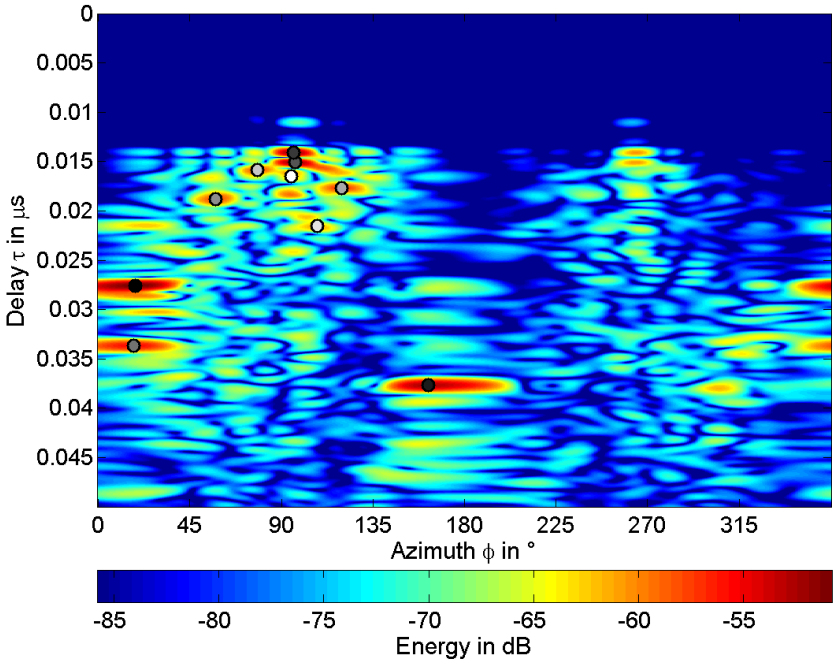

Figure 5.24: Result for 10x3 antenna array, B = 2000MHz.

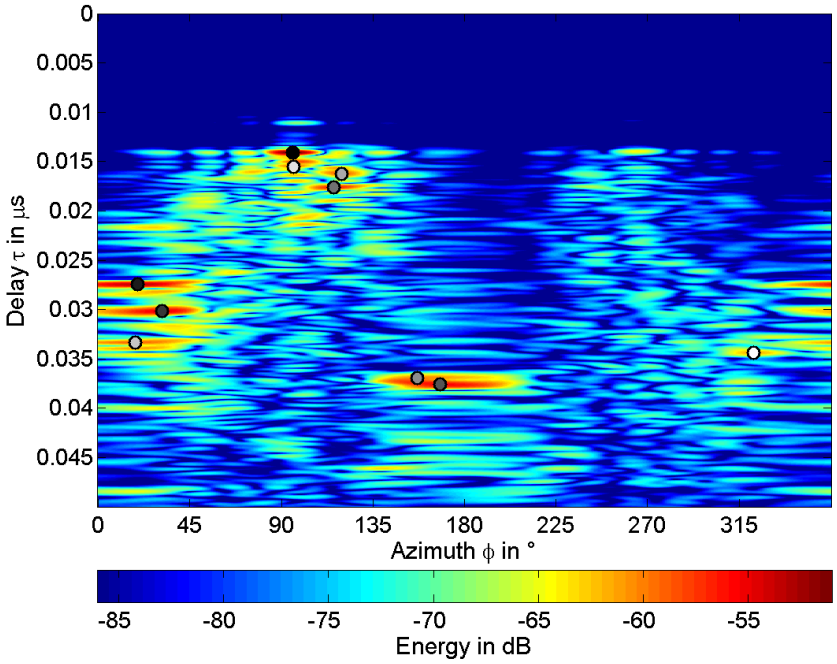

Figure 5.25: Result for 10x3 antenna array, B = 4000MHz.

Comparing these plots, it turns out that in this environment the results are not as clear as in the LOS case. Strong waves are detected for every bandwidth at about 14ns impinging at the receiver array from 95°, originating from a reflection on the ceiling, and at 27ns from the wall to the right with 25°. At 37ns a reflection from the wall to the left of the array, with an angle of 170°, is estimated for bandwidths larger than 1000MHz. The MPC arriving at 14ns is in all cases followed by a few weak waves from angles between 50° and 130°. With 1000MHz bandwidth a strong wave is detected at 30ns from 30°, while with 2000MHz at 34ns a wave impinging from 25° is found. Both these reflections from the wall to the right are also estimated at the largest bandwidth 4000MHz.

For interpretation and verification of these results it is reasonable to take a look at the magnitude-delay profiles in Figure 5.21. Five clearly distinguishable MPCs can be observed propagating through the receiver grid, the rest of the received energy can not be definitely assigned to deterministic MPCs. The distinctive waves match the ones estimated with the 4000MHz bandwidth. Only two of them are detected with 500MHz bandwidth, which is caused by the lower temporal solution. At 1000MHz and 2000MHz bandwidth the algorithm fails to locate one of the MPCs. Hence, for environments with a large amount of diffuse scattering, it is advisable to use large signal bandwidths to obtain reliable results. Figure 5.26 shows a possible interpretation of the reflection paths.

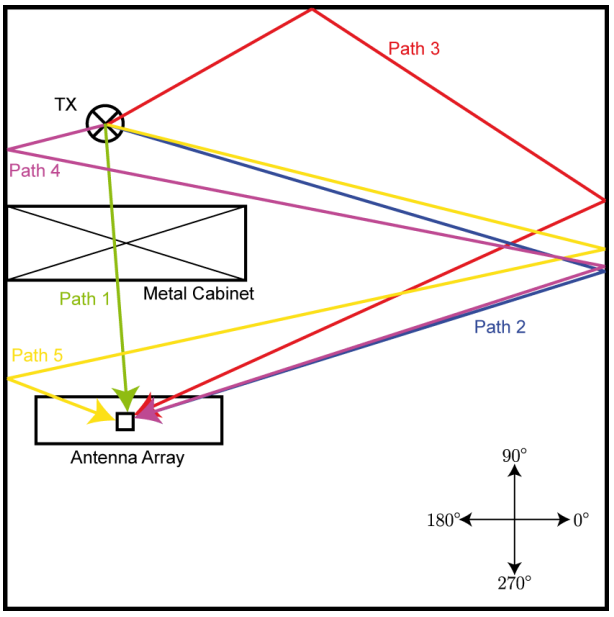

Figure 5.26: Strongest detected waves.

When comparing the average energy captured in the estimation process to the average received energy in Table 5.2, the same observation as in the analyzed LOS case can be made. The average captured energy decreases with signal bandwidth and array size. In addition to that, the percentage of captured energy is significantly lower than in the LOS case. The reason for that is that a lot of energy lies in diffuse MPCs and is therefore not captured. Furthermore, the deterministic waves themselves carry less energy than in the LOS scenario. As the average captured energy for the 10x10 antenna array falls below 13% for all bandwidths, it is again pointed out that in this environment a smaller antenna array is more suitable.

Bandwidth	10x2 Array	10x3 Array	10x10 Array
500MHz	55.21%	45.23%	11.83%
1000MHz	48.95%	40.04%	11.98%
2000MHz	38.86%	32.84%	12.69%
4000MHz	24.48%	20.96%	8.01%

Table 5.2: Average energy captured by estimation in percent of average received energy.

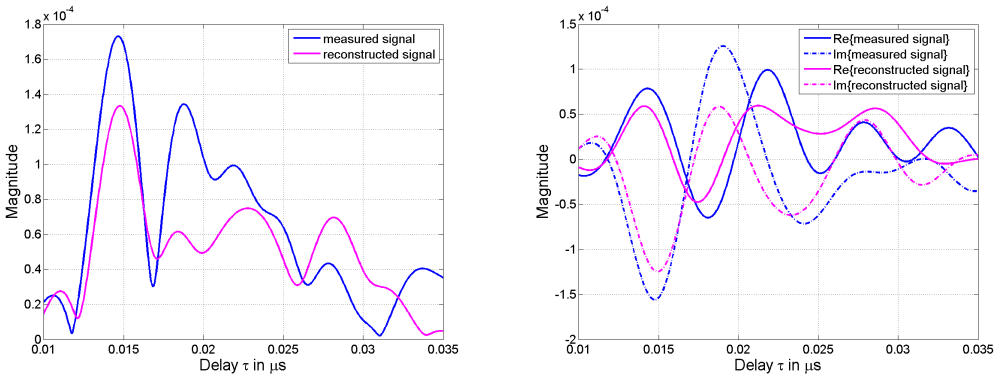

(a) Magnitude representation. (b) Real/Imaginary part representation.

Figure 5.27: Received and reconstructed signal for B = 500MHz.

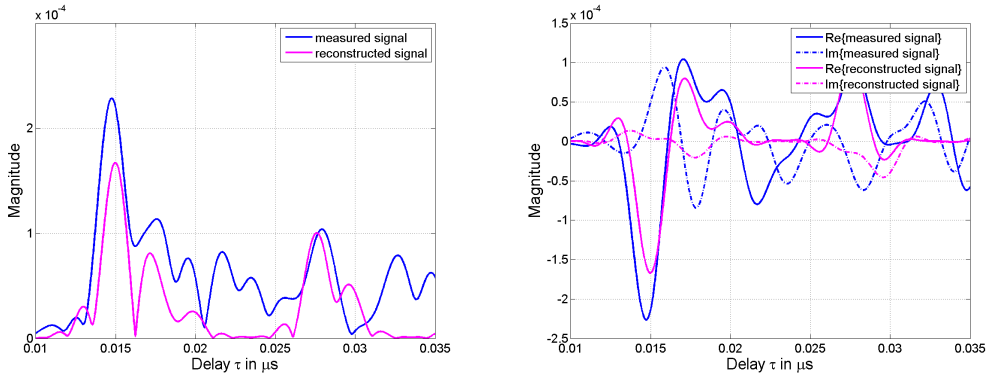

(a) Magnitude representation. (b) Real/Imaginary part representation.

Figure 5.28: Received and reconstructed signal for B = 1000MHz.

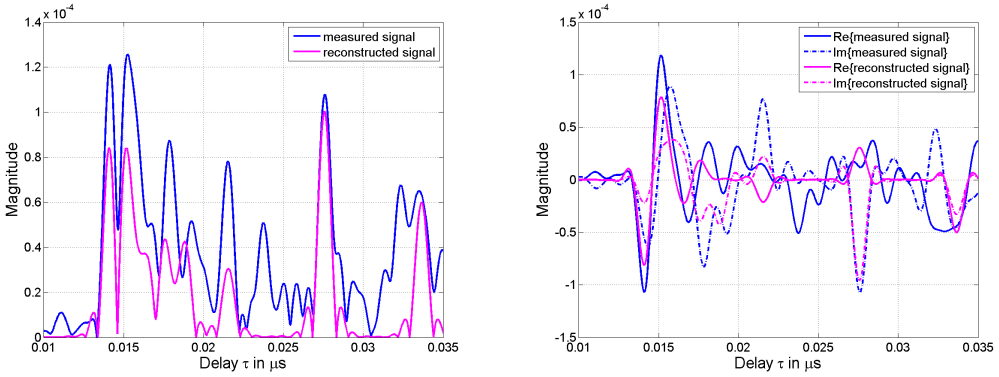

(a) Magnitude representation. (b) Real/Imaginary part representation.

Figure 5.29: Received and reconstructed signal for B = 2000MHz.

As in the previous Section, the received signals for a specific antenna are reconstructed and compared to the actually received signals. Figures 5.27–5.30 show the results. Obviously, the results are not as accurate as for the LOS scenario. The reason for that is again the amount of scattering in the measurement environment. Nevertheless, the results are still usable, as is proven by the reconstruction of the magnitude-delay profiles for adjoining antennas parallel to the x-axis in Figures 5.31–5.34. These plots demonstrate that the results enable an acceptable approximation to the received signals. Deterministic paths can be clearly recognized and assigned to their source in the magnitude-delay profiles for the received signals. Best results are achieved with the high temporal resolution provided by the 4000MHz signal.

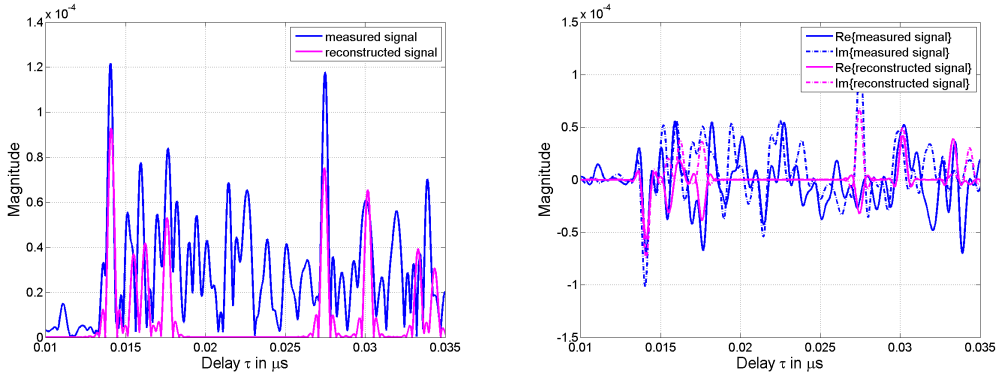

(a) Magnitude representation. (b) Real/Imaginary part representation.

Figure 5.30: Received and reconstructed signal for B = 4000MHz.

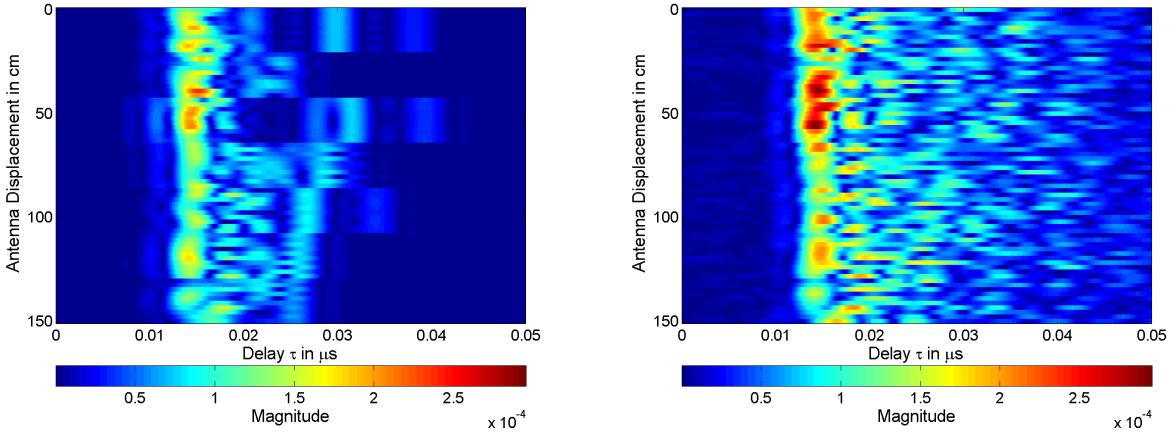

(a) Reconstructed signals. (b) Received signals.

Figure 5.31: Propagation of waves through measurement grid for B = 500MHz.

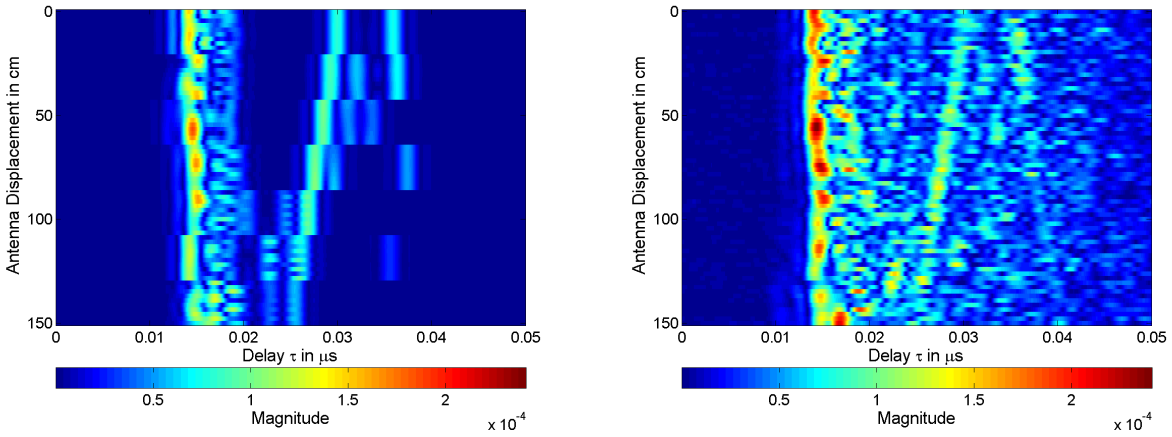

(a) Reconstructed signals.

(b) Received signals.

Figure 5.32: Propagation of waves through measurement grid for B = 1000MHz.

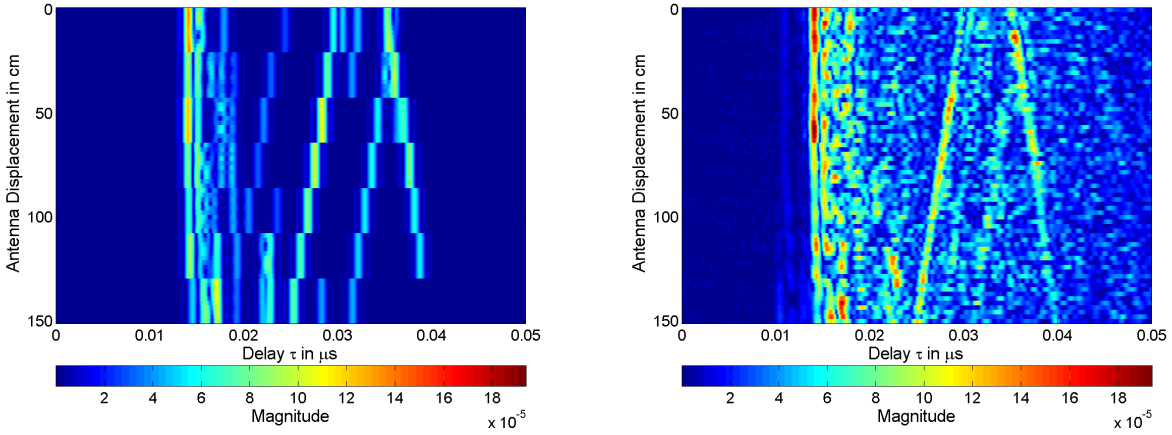

(a) Reconstructed signals.

(b) Received signals.

Figure 5.33: Propagation of waves through measurement grid for B = 2000MHz.

The presented results emphasize that excellent temporal resolution is required to extract parameters correctly in environments that are characterized by a multitude of diffuse scattering processes. A comparison of the 4000MHz received signal magnitude-delay profiles in Figure 5.34b with the magnitude-delay profiles arising from signals reconstructed from an estimation process using a 10x10 antenna array in Figure 5.35 points out that it is important to keep that fact in mind when choosing the size of the antenna array. Even though the deterministic MPCs are detected, the energy distribution can not be approximated as well as for smaller arrays. Time gating for such large arrays lowers the

temporal resolution significantly, and can therefore reduce the advantages gained by the use of large bandwidths.

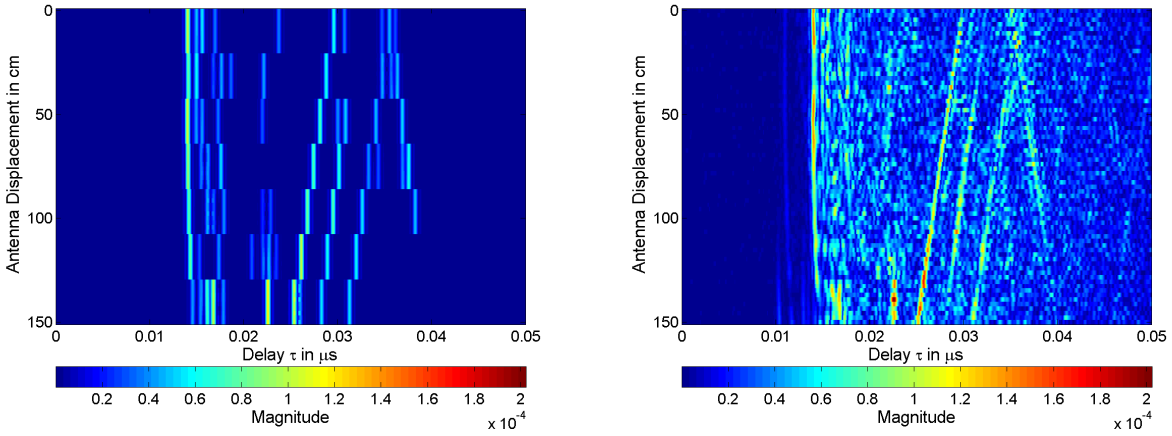

(a) Reconstructed signals.

(b) Received signals.

Figure 5.34: Propagation of waves through measurement grid for B = 4000MHz.

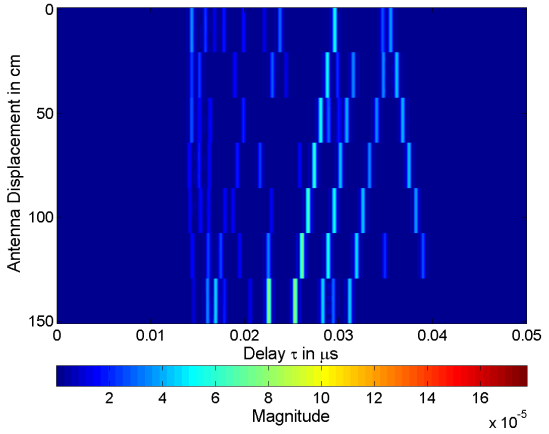

Figure 5.35: Reconstructed magnitude-delay profiles for 10x10 antenna array, B = 4000MHz.

5.2 Measurement Analysis 2

In this Section, measurement data that was taken by Christian Unterkofler for his Master's Thesis [Unt09] is analyzed. The measuring system was set up at different locations at the Signal Processing and Speech Communication Laboratory [SPS] at Graz University

of Technology [tug]. It is again assumed that the antenna used for the measurements is omnidirectional, so that $f_m(\phi, \psi) = 1$ for $m = 1, \ldots, M$.

In each of the two analyzed scenarios the transmitter antenna was placed in a fixed position and the receiver antenna was moved in steps of 1cm in a 3x41x35 grid for the first scenario, and a 1x41x35 grid for the second scenario. These antenna arrangements were chosen in order to enable resolution of azimuth angles as well as elevation angels. As the work in [Unt09] concentrated on the characteristics of reflected waves only, the LOS paths between transmitting and receiving antenna were attenuated by radio frequency absorbers, so that the energy carried by the direct path would not outshine the reflections.

Like for the previously analyzed measurements, UWB pulse transmission is simulated for different bandwidths for antenna arrays at several adjoining positions in the available measurement grid. Spacing between the antennas is again chosen to be 2cm, so that the upper frequency band-edge of the transmitted pulse has to be 7500MHz.

5.2.1 Lecture Hall

For the first scenario, a lecture hall of about 10m height with very little inventory was chosen as measurement environment. The transmitter antenna was positioned between the blackboard and the first seat row at 0.75m height and the origin of the receiver antenna array was positioned at a height of 1m with a distance of 2.2m from the transmitter antenna. An aluminium foil covered ball was placed in front of the blackboard. The measurement setup is illustrated in Figure 5.36.

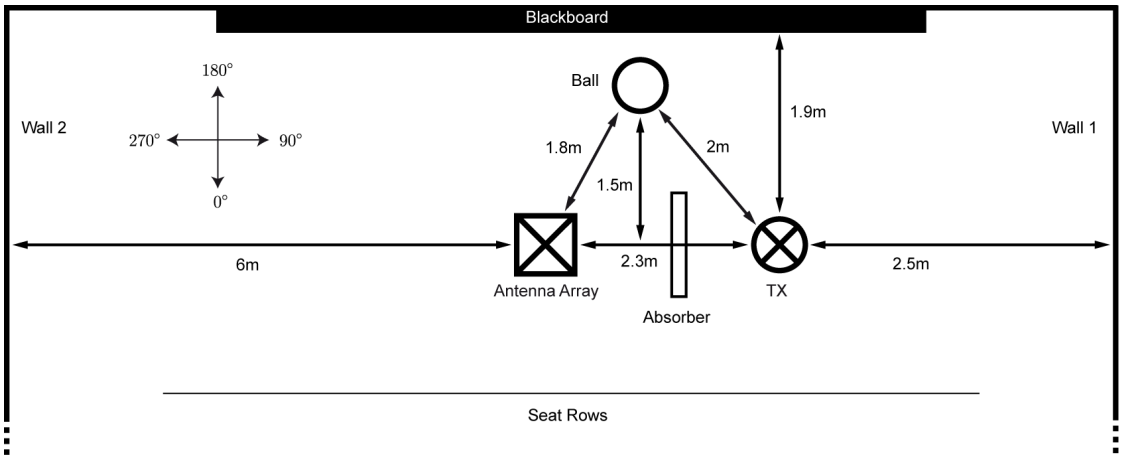

Figure 5.36: Measurement setup lecture hall [Unt09].

Since the dimensions of the lecture hall are larger than the dimensions of the office, where the measurements analyzed in Section 5.1 were taken, the channel is expected to be characterized by a much longer delay spread and weaker deterministic MPCs because reflected waves have to travel long distances before reaching the receiver.

To illustrate the estimated delays, azimuth and elevation angles of the MPCs, the detected paths are plotted across the azimuth-delay scattering function $S(\tau, \phi)$ and the elevation-delay scattering function $S(\tau, \psi)$ arising from the associated measurement array. As elevation angles are also considered in this measurement analysis, the azimuth-delay scattering function in (5.1) has to be adjusted to include all considered elevation angles. The angle-delay scattering functions are computed by [PNG08], [CPD09]

$$S(\tau, \phi) = \left| \sum_{m=1}^{M} \sum_{\psi} Y_m(\tau) e^{-j2\pi\lambda^{-1}(\Delta x_m \cos\psi \cos\phi + \Delta y_m \cos\psi \sin\phi + \Delta z_m \sin\psi)} \right|^2 \tag{5.2}$$

and

$$S(\tau, \psi) = \left| \sum_{m=1}^{M} \sum_{\phi} Y_m(\tau) e^{-j2\pi\lambda^{-1}(\Delta x_m \cos\psi \cos\phi + \Delta y_m \cos\psi \sin\phi + \Delta z_m \sin\psi)} \right|^2 . \tag{5.3}$$

In Figures 5.38–5.40 the results obtained with a 2x10x3 array for bandwidths 500MHz, 2000MHz and 4000MHz are presented. The number of paths is set to 20. The results are obviously not as unambiguous as for the previously analyzed measurements. Strong reflections from the aluminium foil covered ball, impinging at the receiver at 11ns from azimuth angle 145° and elevation angle around 0°, are detected for all three bandwidths. Only two other waves are estimated for all bandwidths: another reflection from the ball and a reflection from the wall behind the receiver (Wall 2) reaching the receiver at 60ns from azimuth angle 270° with elevation 0°. The LOS and the first reflection from the wall behind the transmitter (Wall 1), both arriving from azimuth angle 90°, are estimated with the larger bandwidths, but not at 500MHz. This may be explained by the fact that a larger amount of used frequencies increases the probability that an obstacle, in this case the RF-absorber, is penetrated.

A summary of the estimated waves, their delays, incident angles and reflection points, as well as the bandwidths they are estimated with, can be found in Table 5.3. Figure 5.37 illustrates a possible interpretation of the results.

MPC	τ	ϕ	ψ	reflection point	500MHz	2000MHz	4000MHz
1	7ns	90°	0°	LOS		X	X
2	11ns	145°	0°	Ball	X	X	X
3	12ns	35°	0°	1st Seat Row	X	X	
4	22ns	145°	0°	Ball	X	X	X
5	25ns	90°	0°	Wall 1		X	X
6	45ns	90°	50°	Ceiling	X	X	
7	60ns	270°	0°	Wall 2	X	X	X
8	95ns	90°	0°	Wall 1	X	X	

Table 5.3: Estimated MPCs in the lecture hall.

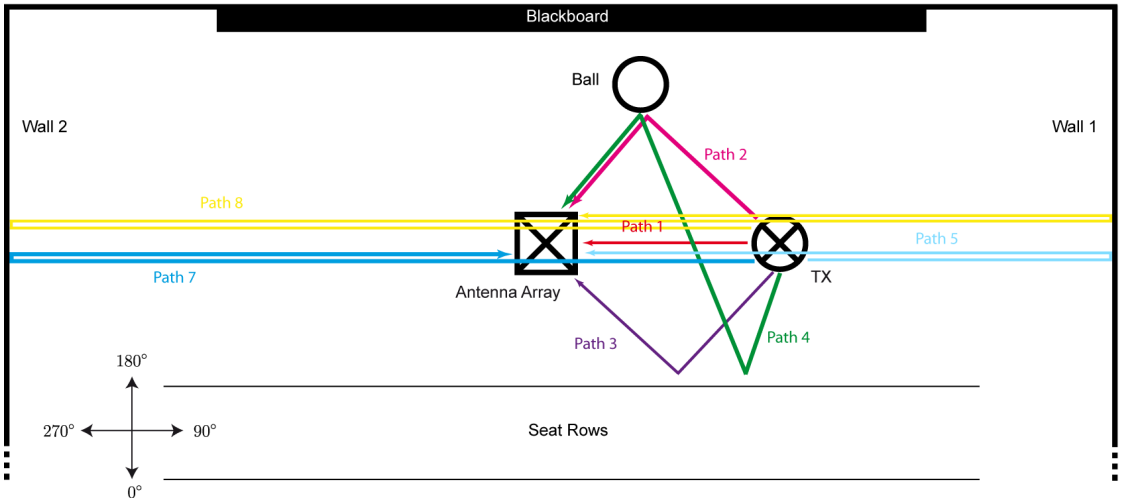

Figure 5.37: Detected waves lecture hall.

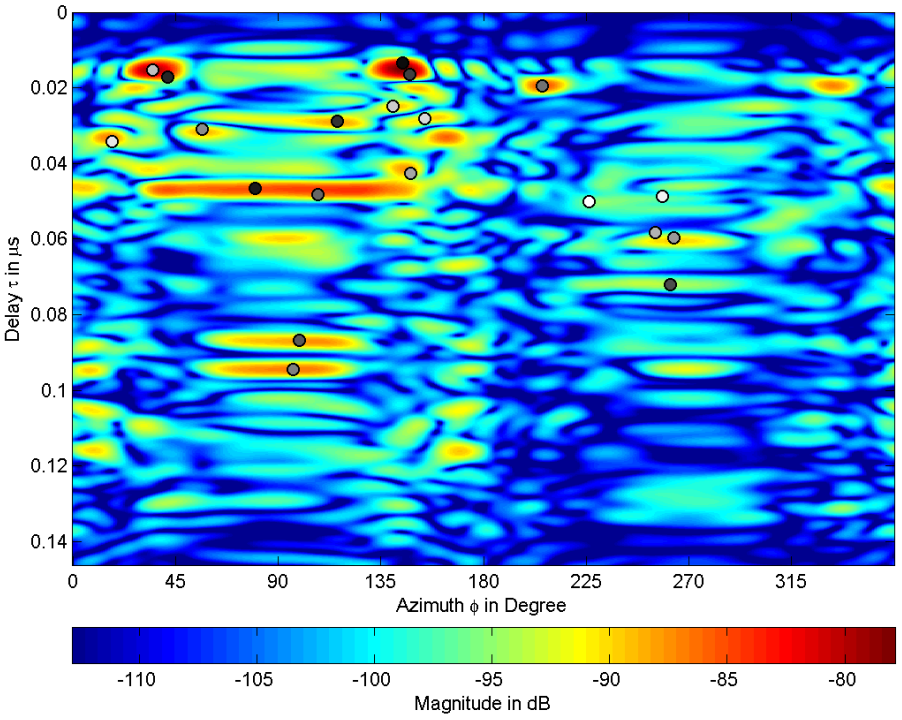

(a)

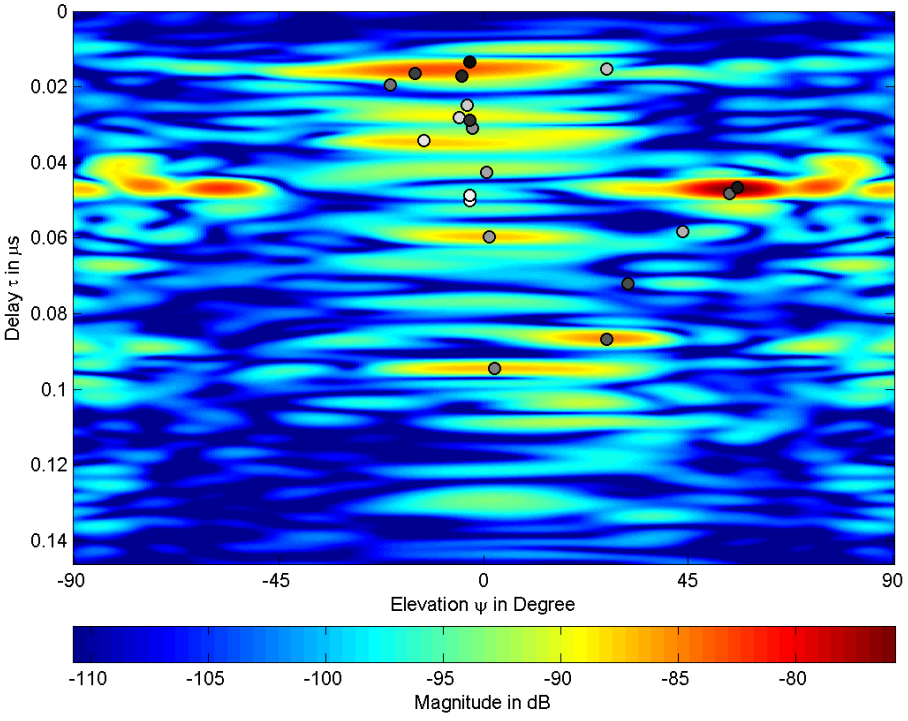

(b)

Figure 5.38: Result for 2x10x3 antenna array, B = 500MHz.

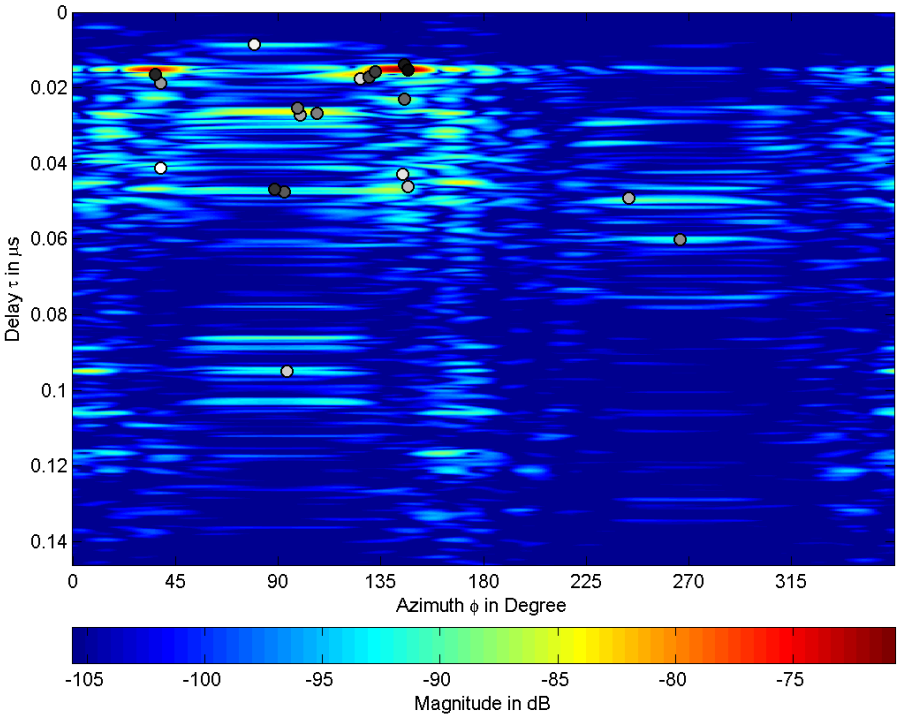

(a)

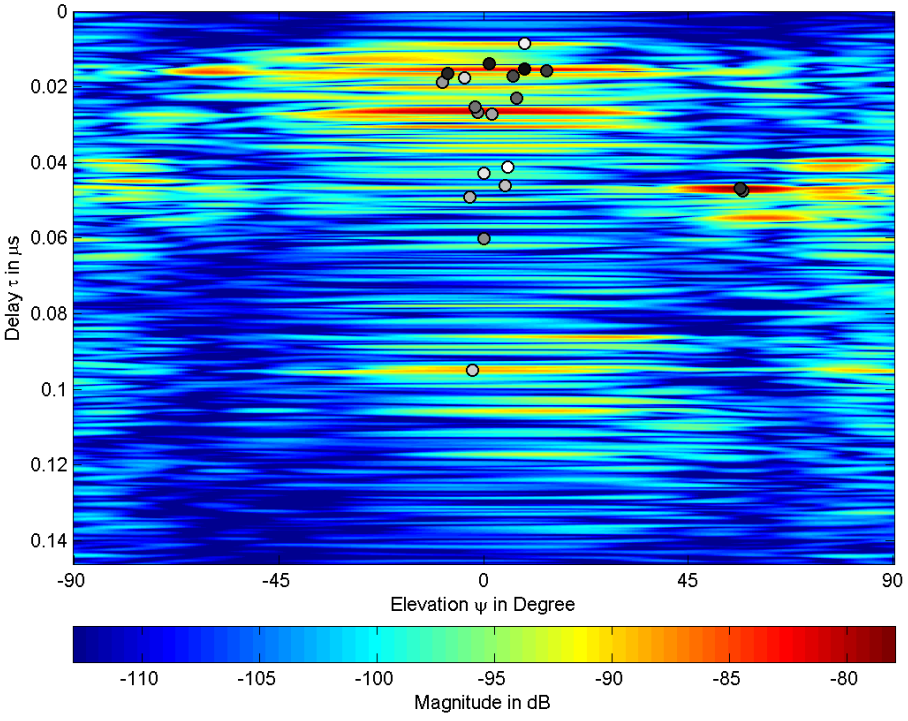

(b)

Figure 5.39: Result for 2x10x3 antenna array, B = 2000MHz.

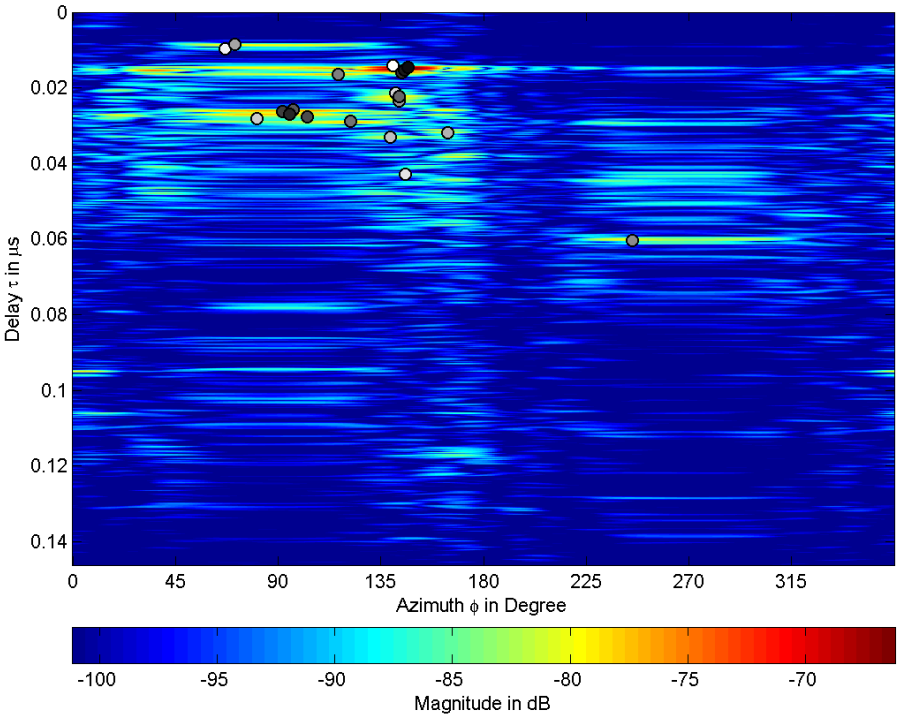

(a)

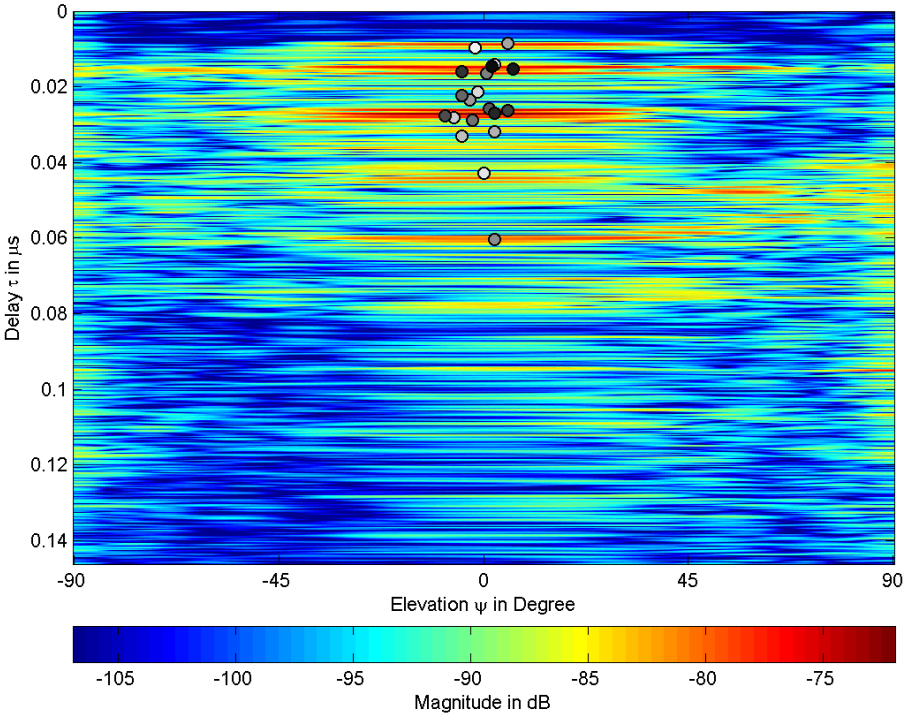

(b)

Figure 5.40: Result for 2x10x3 antenna array, B = 4000MHz.

The average energy captured in the estimation procedure in percent of the received energy follows, as expected, the same pattern as for the other measurements. For smaller bandwidths the estimated waves carry more energy compared to the received energy than the MPCs estimated for larger bandwidths. The average captured energy for 500MHz bandwidth is 48.51%, for 2000MHz it is 29.29%, while for 4000MHz only 23.37% of the received energy are captured.

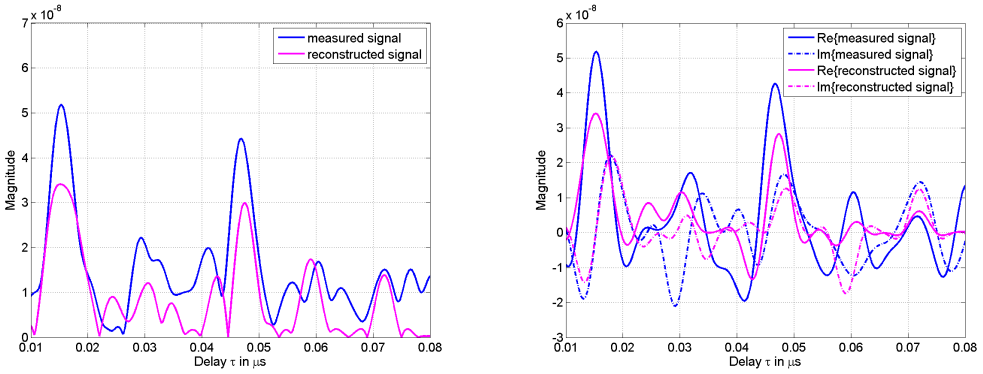

(a) Magnitude representation. (b) Real/Imaginary part representation.

Figure 5.41: Received and reconstructed signal for B = 500MHz.

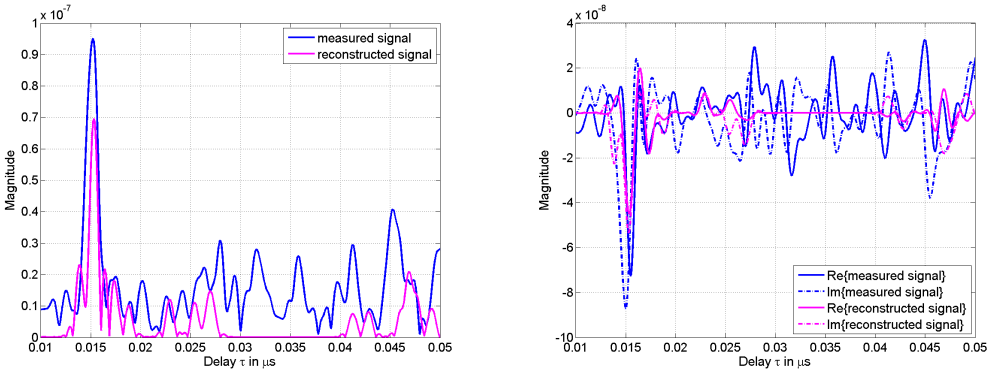

(a) Magnitude representation. (b) Real/Imaginary part representation.

Figure 5.42: Received and reconstructed signal for B = 2000MHz.

For the demonstration of the estimated complex amplitudes, reconstructed signals at a specific antenna within the array for all three bandwidths are illustrated in Figures 5.41–5.43. To visualize the results as best as possible, the delay-axis is restricted to an appropriate time span. The Figures show that the channel can be approximated

sufficiently well for all three bandwidths. For 500MHz real and imaginary parts of the reconstructed signal match the received signal, while for the larger bandwidths the same can be observed as for the previously analyzed measurements. The better the temporal resolution, the more stochastic components become visible in the received signal but are not present in the reconstructed signal.

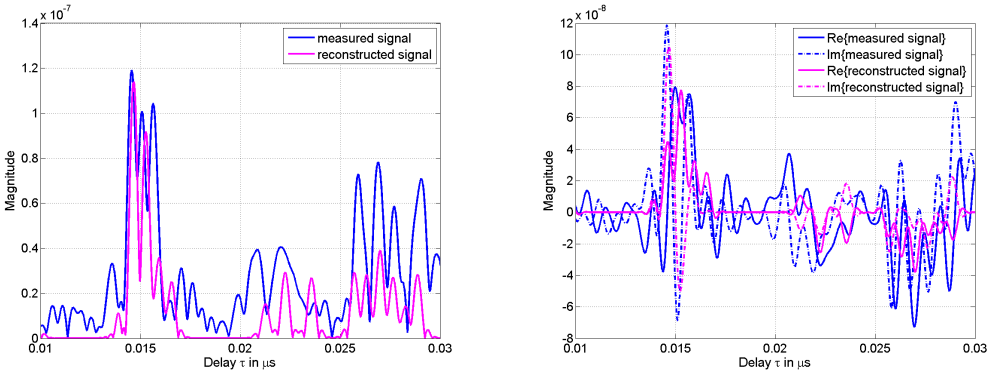

(a) Magnitude representation.

(b) Real/Imaginary part representation.

Figure 5.43: Received and reconstructed signal for B = 4000MHz.

Propagation of the detected MPCs through the measurement grid is visualized in Figures 5.44–5.45. Since the antenna array for the measurement analysis in this Subsection is 3-dimensional, wave propagation is shown by reconstruction of signals at adjoining antennas in y- as well as in z-direction for all bandwidths. The Figures offer an explanation as to why the results obtained for the measurements in this Subsection are not as unambiguous as the results analyzed in the previous Section. A visual comparison of the magnitude-delay profiles for the received signals in Figures 5.44b–5.45f to the magnitude-delay profiles for the received signals in Figures 5.14b–5.17b and 5.31b–5.34b shows that the channel in this Subsection is characterized by a lot of stochastic components, which makes it hard to identify deterministic MPCs, while in the plots from the previous Section the propagation paths of deterministic waves through the measurement grid are clearly distinguishable from the noise. Nevertheless, the results for all bandwidths exhibit similar patterns as those that can be observed in the received signals. The MPCs that are indicated in the received magnitude-delay profiles are also present in the estimated profiles.

Even though the results are not as accurate as those obtained for the measurements analyzed in Section 5.1, it can be concluded from the obtained results that the algorithm successfully extracts deterministic MPCs from the measurement data for all considered bandwidths.

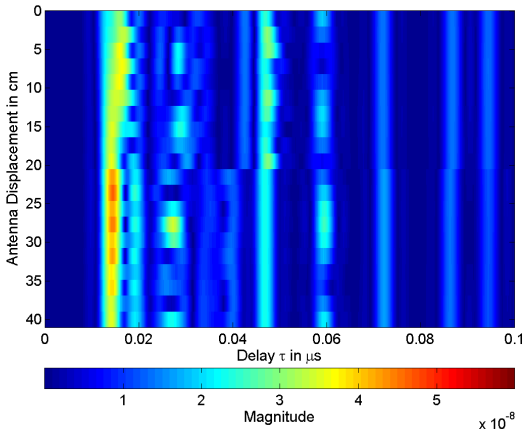

(a) Reconstructed signals, B = 500MHz.

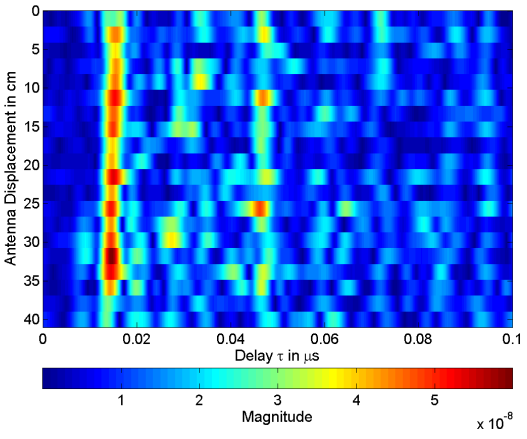

(b) Received signals, B = 500MHz.

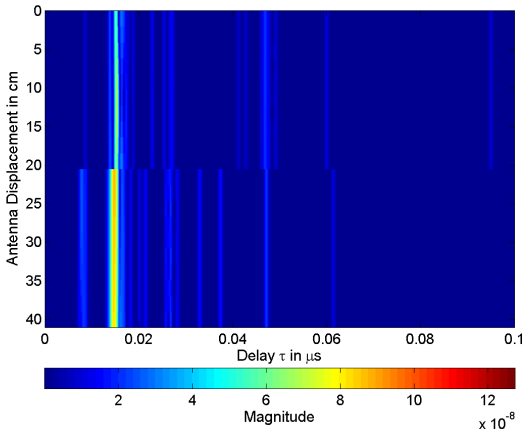

(c) Reconstructed signals, B = 2000MHz.

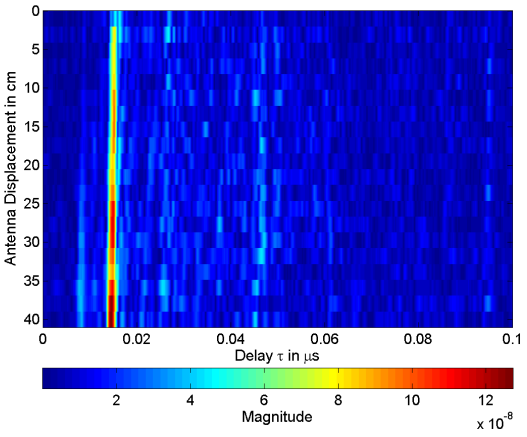

(d) Received signals, B = 2000MHz.

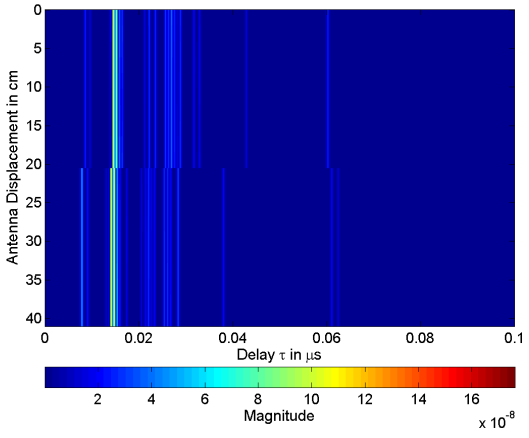

(e) Reconstructed signals, B = 4000MHz.

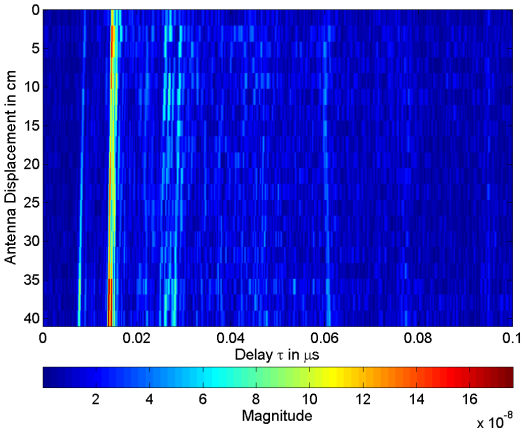

(f) Received signals, B = 4000MHz.

Figure 5.44: Propagation of waves in y-direction.

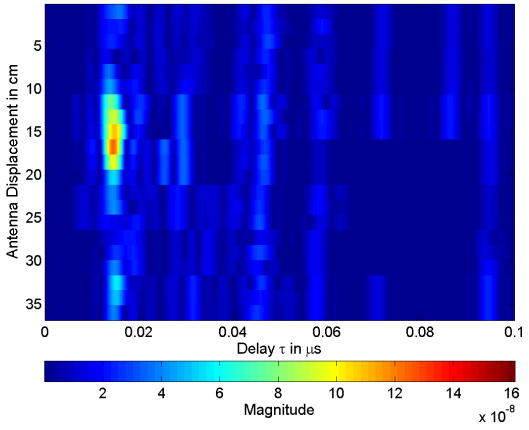

(a) Reconstructed signals, B = 500MHz.

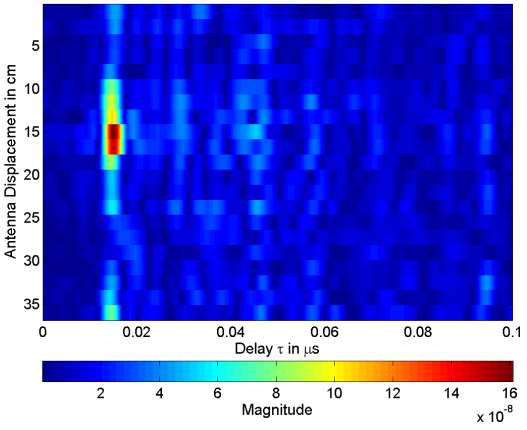

(b) Received signals, B = 500MHz.

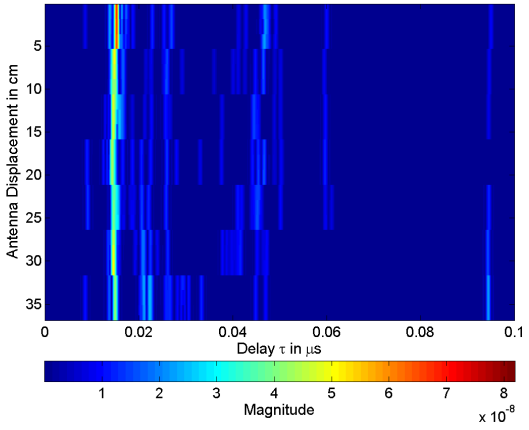

(c) Reconstructed signals, B = 2000MHz.

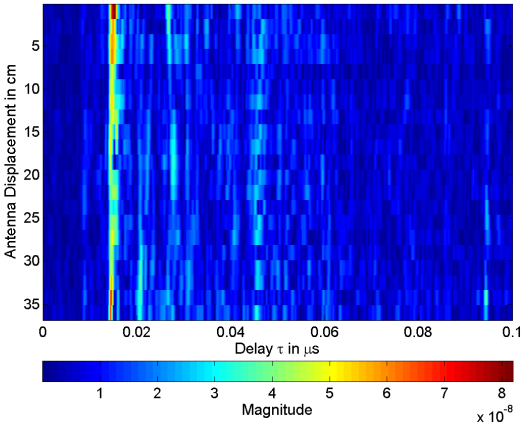

(d) Received signals, B = 2000MHz.

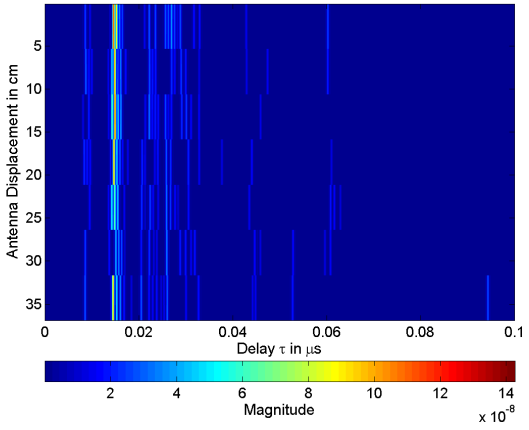

(e) Reconstructed signals, B = 4000MHz.

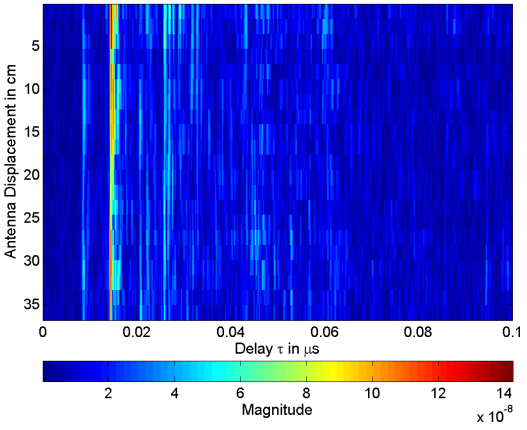

(f) Received signals, B = 4000MHz.

Figure 5.45: Propagation of waves in z-direction.

5.2.2 Computer Lab

The measurement data analyzed in this Subsection was acquired in a computer lab. The lab is an environment with a lot of inventory like desks, computers and monitors. The channel can therefore be expected to be characterized by mainly stochastic components and MPCs that are closely spaced in time, which makes the computer lab a very challenging environment for parameter estimation.

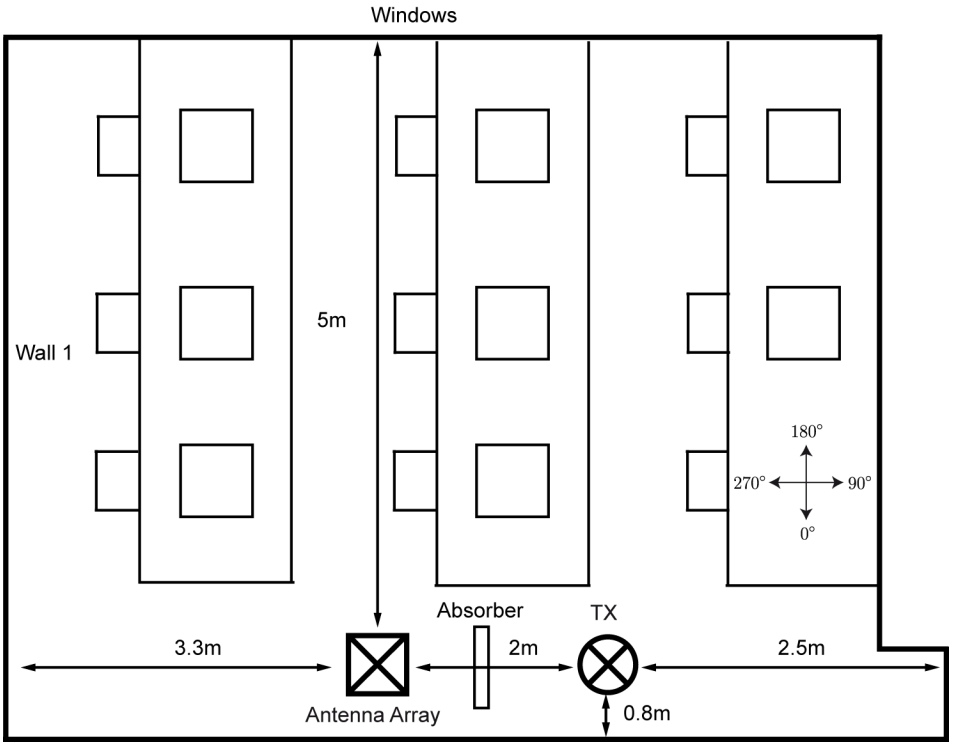

Figure 5.46: Measurement setup computer lab [Unt09].

For the measurements, transmitting antenna and receiver array were positioned 2m apart from each other, rather close to a wall and the inventory. The measurement setup is depicted in Figure 5.46. Since the measurement grid was chosen to be 1x41x35cm, the antenna array for UWB pulse transmission simulation is chosen to be 1x10x3, so that again results can be obtained for several arrays positioned next to each other. Using only one line of antennas in x-direction is of course suboptimal for the parameter estimation procedure, since this limits the resolvable azimuth range [Van02]. The range of azimuth angles considered for parameter estimation has therefore to be confined to the interval $\left[-\frac{\pi}{2}, +\frac{\pi}{2}\right]$. Azimuth angles outside this interval are estimated as if mirrored on the y-axis. This makes it harder to interpret the results of the estimation procedure.

Figures 5.48–5.50 illustrate the results obtained for bandwidths 500MHz, 2000MHz

and 4000MHz with the number of MPCs set to 20. Again, the results are not very clear. The LOS reaches the receiver at 6ns from azimuthal direction 90° and elevation angle 0°. With 2000MHz bandwidth it is correctly estimated, while with bandwidths 500MHz and 4000MHz the azimuth angle is estimated between 20° and 30° off. The LOS is followed by a cluster of MPCs, arriving between 10ns and 23ns from azimuth angles between 45° and 90° with elevation between −50° and 0°. Single waves of this cluster cannot be definitely assigned to specific reflection points. The MPCs are reflections of the floor (90° azimuth, −50° elevation) and inventory (metal legs of desks, computer, monitor). At about 35ns a reflection from the wall behind the receiver (Wall 1) reaches the array and at 40ns a wave reflected by the metal frames of the windows impinges. A summary of impinging MPCs can be found in Table 5.4, while Figure 5.47 illustrates the detected waves.

The average captured energy is 67.11% for the 500MHz bandwidth, 41.14% for the 2000MHz bandwidth and 23.61% for the 4000MHz bandwidth.

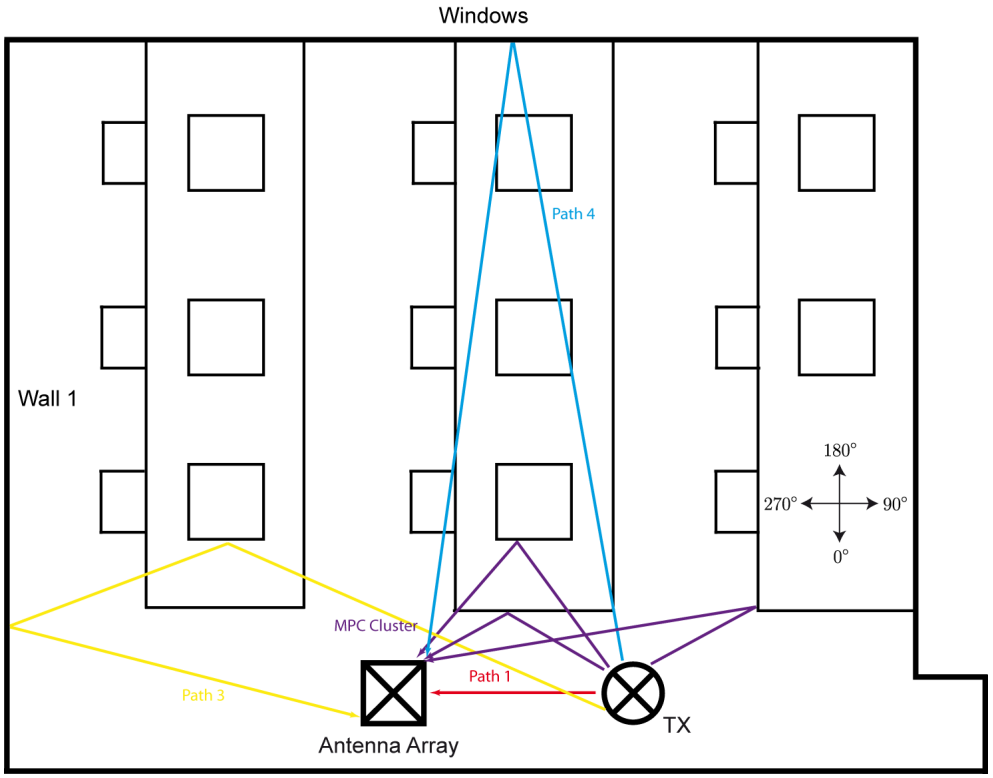

Figure 5.47: Detected waves computer lab.

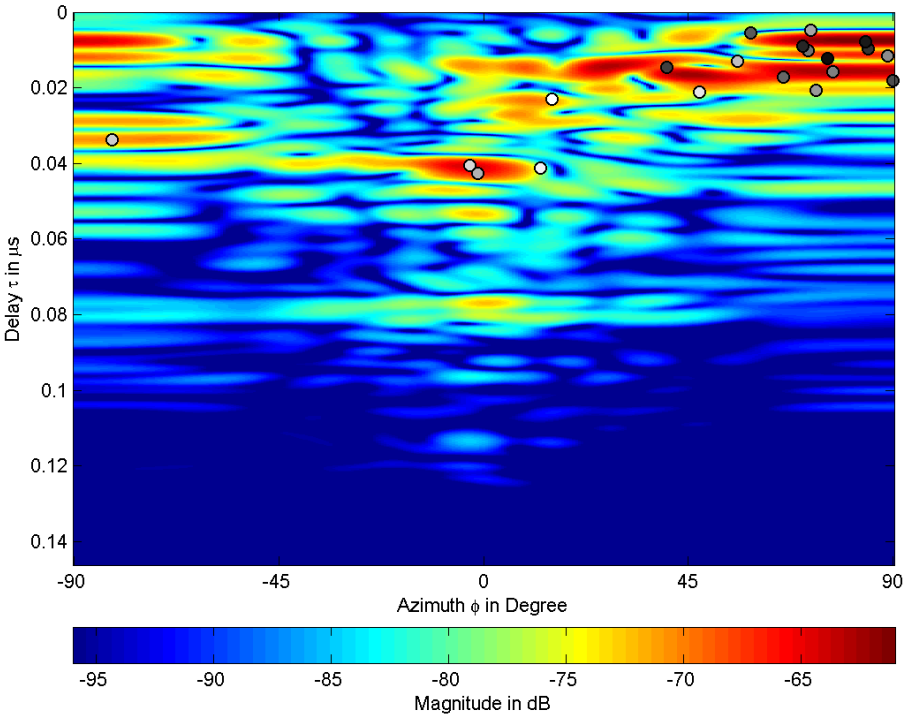

(a)

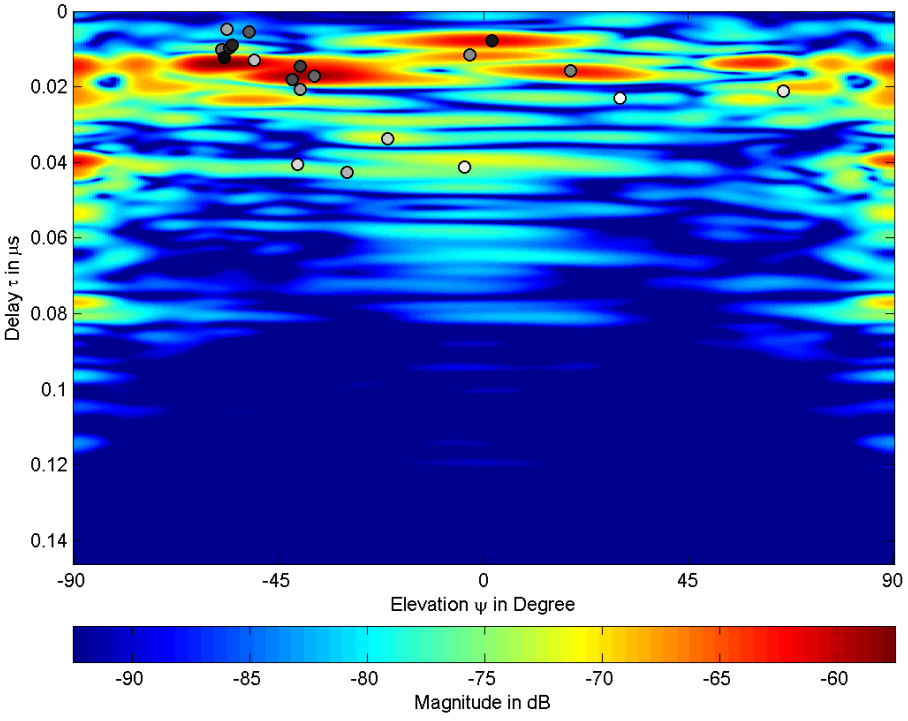

(b)

Figure 5.48: Result for 1x10x3 antenna array, B = 500MHz.

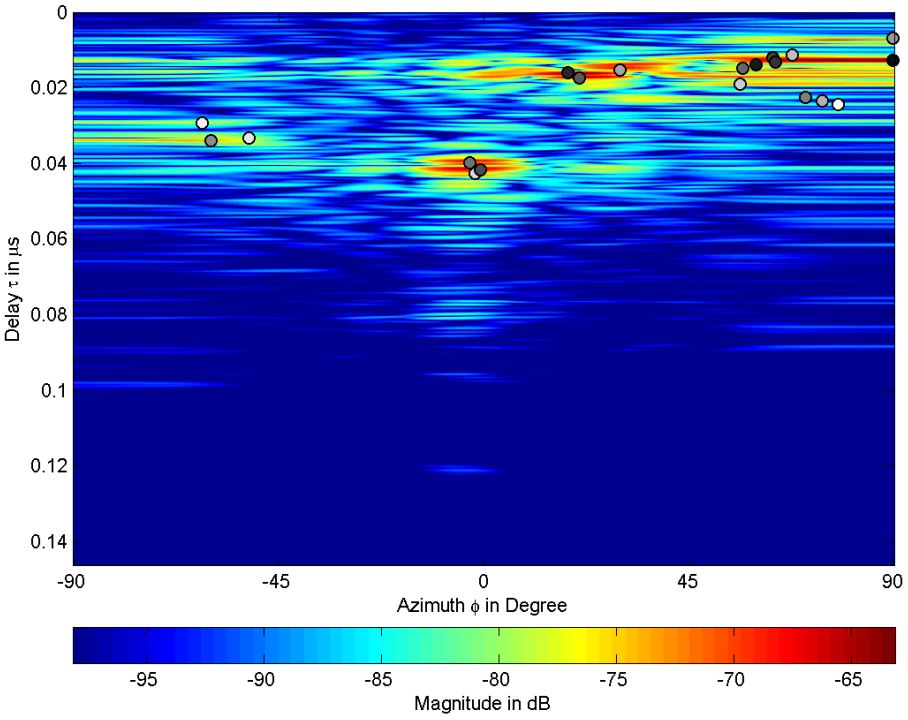

(a)

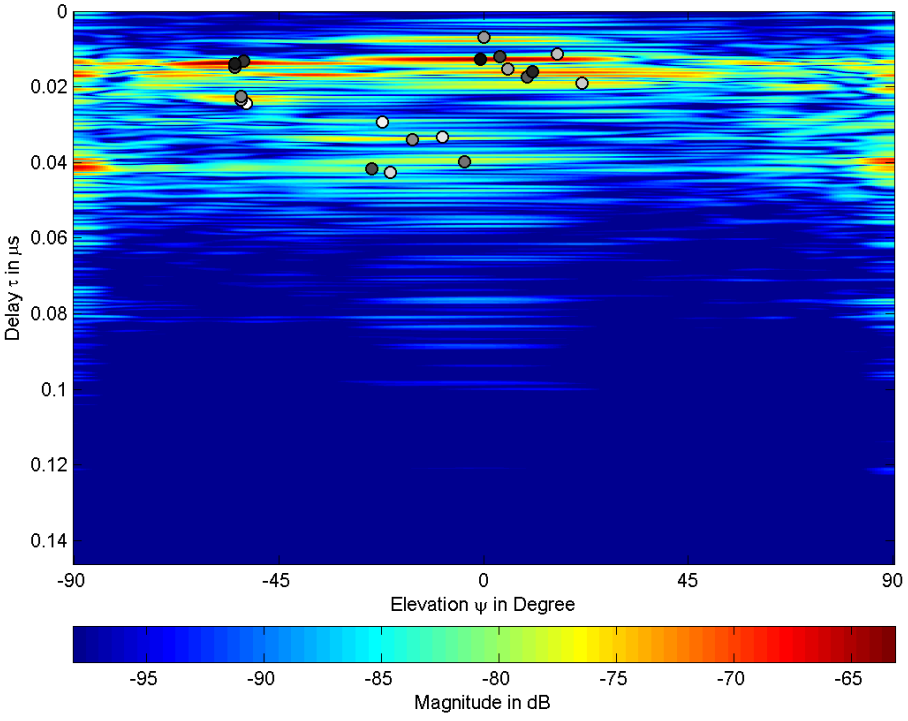

(b)

Figure 5.49: Result for 1x10x3 antenna array, B = 2000MHz.

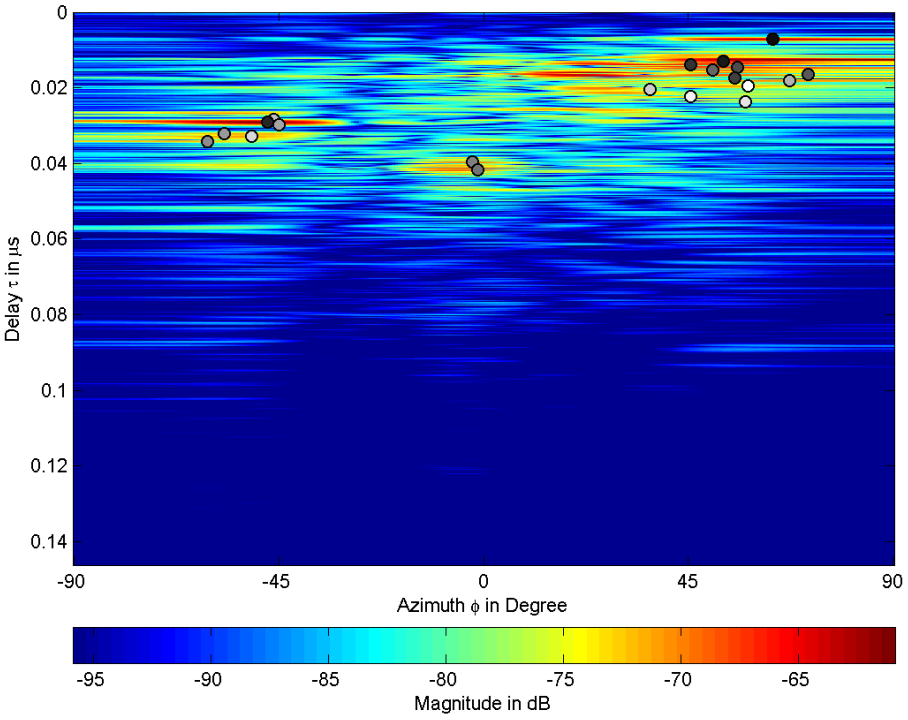

(a)

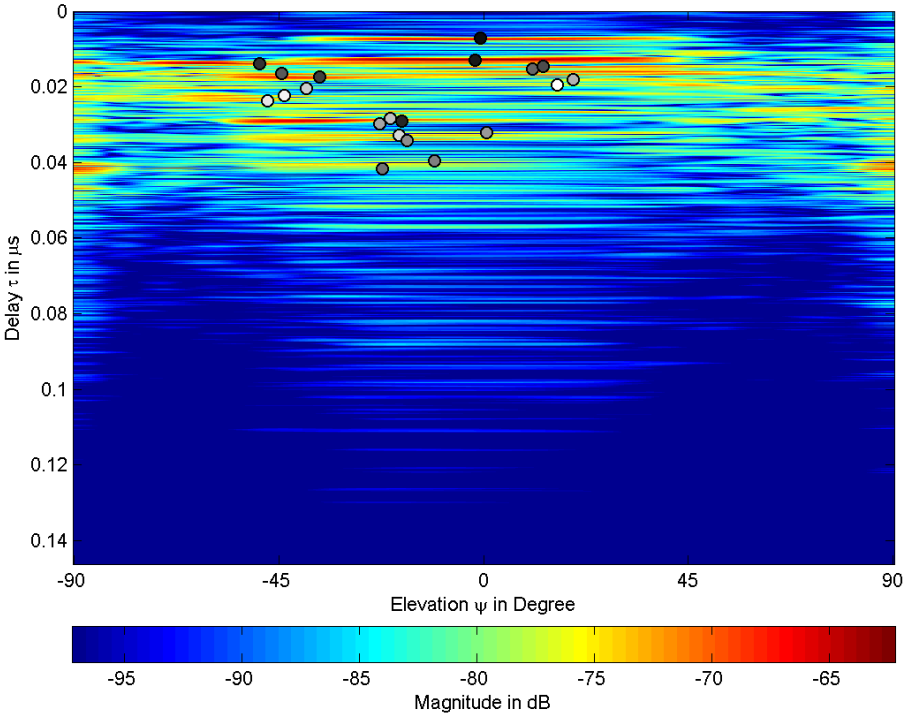

(b)

Figure 5.50: Result for 1x10x3 antenna array, B = 4000MHz.

MPC	τ	ϕ	ψ	reflection point
1	6ns	90°	0°	LOS
MPC Cluster	11ns–23ns	45°–90°	−50°–0°	Floor, Inventory
3	35ns	−55°	−20°	Wall 1
4	40ns	0°	−10°	Window Frame

Table 5.4: Estimated MPCs in the computer lab.

Complex amplitude estimation is illustrated in Figures 5.51–5.53. The delay-axis is again restricted to an appropriate time span to enable the best possible demonstration of the results. Comparison between reconstructed signals and received signals shows that, even though the results are not as accurate as for all previously analyzed measurements, satisfactory channel approximation is achieved for all considered bandwidths. The lack of accuracy may on the one hand result from the especially difficult environment analyzed in this Subsection, and on the other hand from the fact that using an only 2-dimensional antenna array is a fairly suboptimal approach for the combined estimation of azimuth and elevation angles.

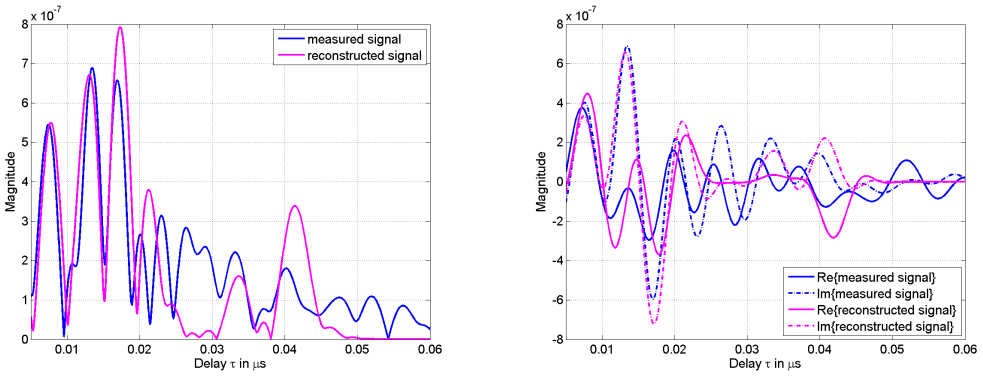

(a) Magnitude representation.

(b) Real/Imaginary part representation.

Figure 5.51: Received and reconstructed signal for B = 500MHz.

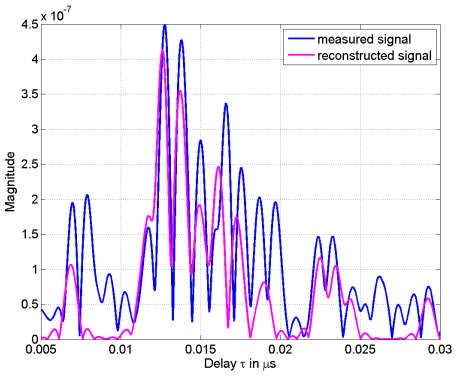

(a) Magnitude representation.

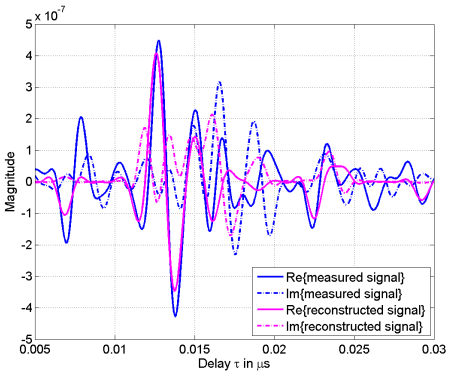

(b) Real/Imaginary part representation.

Figure 5.52: Received and reconstructed signal for B = 2000MHz.

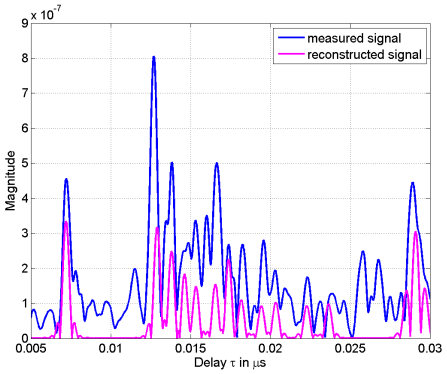

(a) Magnitude representation.

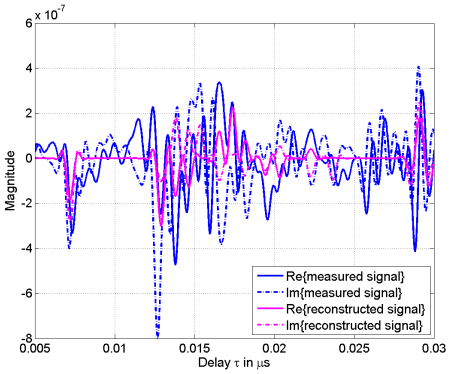

(b) Real/Imaginary part representation.

Figure 5.53: Received and reconstructed signal for B = 4000MHz.

The magnitude-delay profiles of reconstructed and received signals at adjoining antennas in y- as well as in z-direction are visualized in Figures 5.54–5.55. In the plots of the received signals, the cluster of closely-spaced MPCs arriving from quite similar directions is clearly observable. The MPC cluster and other waves are also identifiable in the reconstructed signals plots. As explained before, the algorithm might be overstrained by the complex measurement data and the inadequate approach of using a 2-dimensional array only.

The obtained results for the measurement data in this Subsection do definitely not deliver the high accuracy achieved in the estimation process for the other measurements. This, however, is more due to the nature of the measurement environment and the not quite appropriate antenna array dimension, rather than the proposed algorithm.

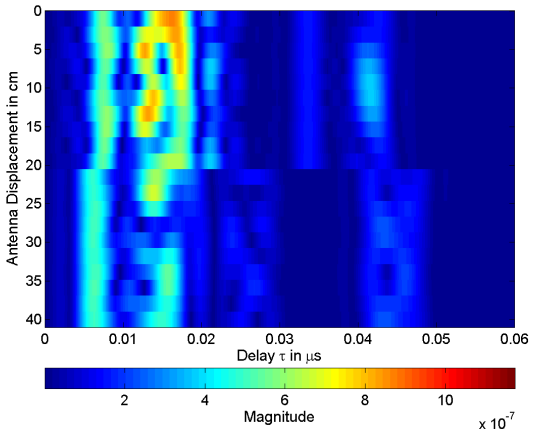

(a) Reconstructed signals, B = 500MHz.

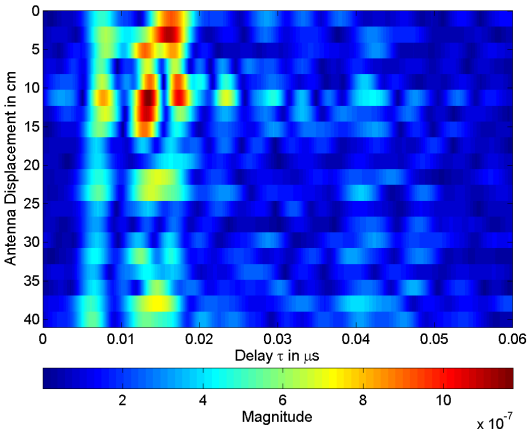

(b) Received signals, B = 500MHz.

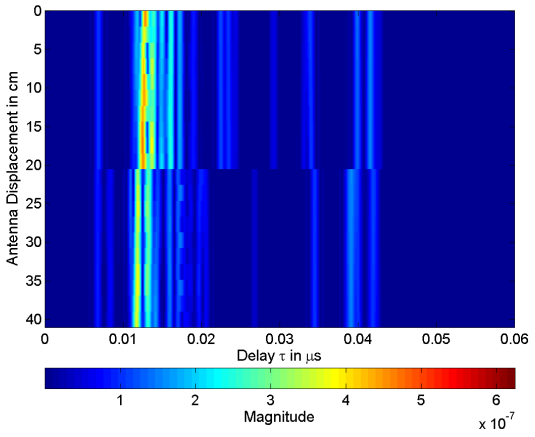

(c) Reconstructed signals, B = 2000MHz.

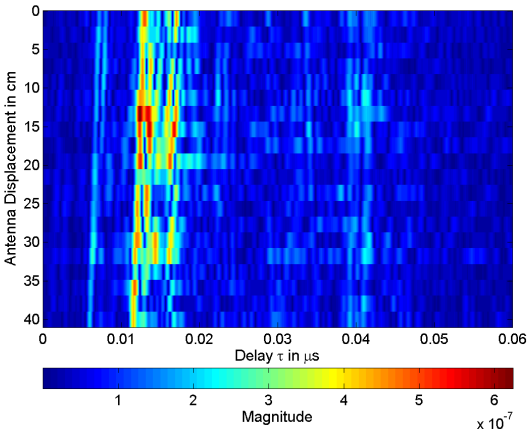

(d) Received signals, B = 2000MHz.

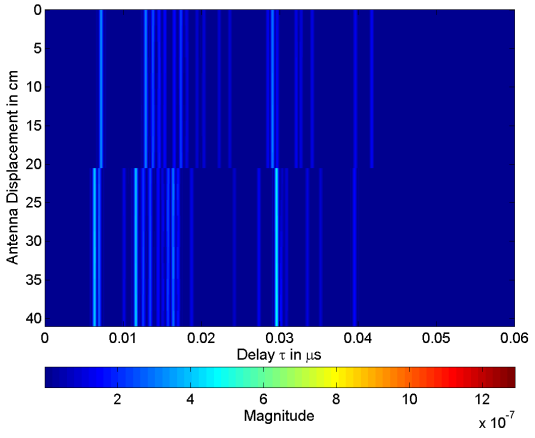

(e) Reconstructed signals, B = 4000MHz.

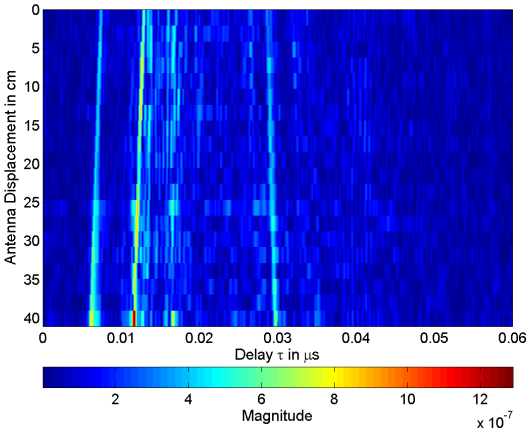

(f) Received signals, B = 4000MHz.

Figure 5.54: Propagation of waves in y-direction.

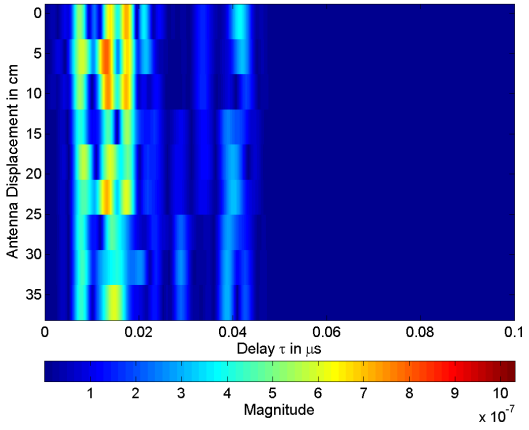

(a) Reconstructed signals, B = 500MHz.

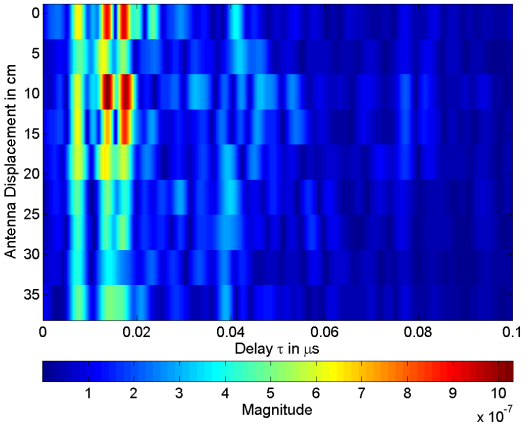

(b) Received signals, B = 500MHz.

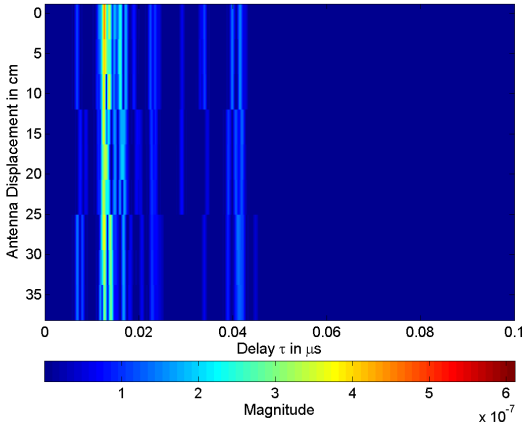

(c) Reconstructed signals, B = 2000MHz.

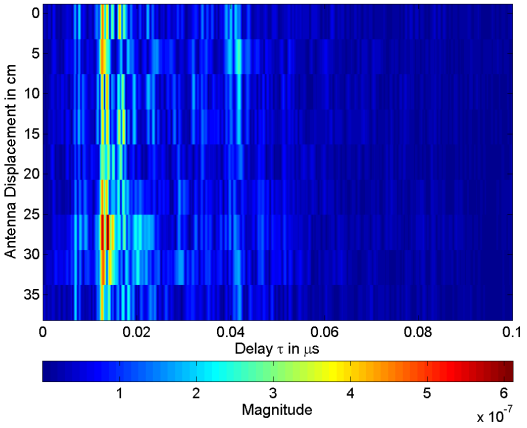

(d) Received signals, B = 2000MHz.

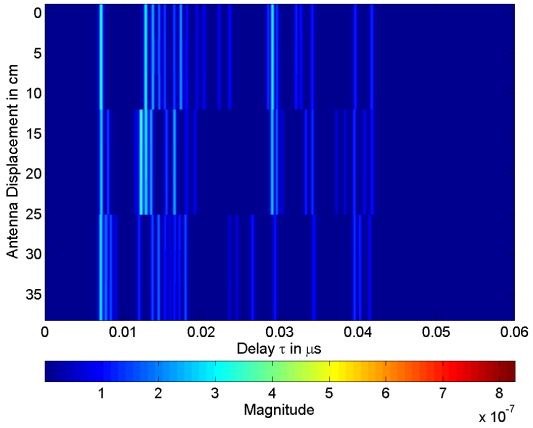

(e) Reconstructed signals, B = 4000MHz.

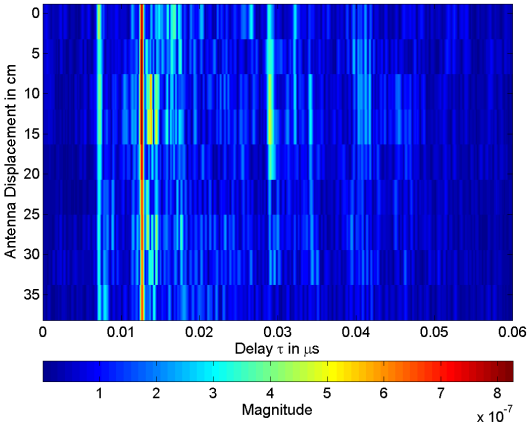

(f) Received signals, B = 4000MHz.

Figure 5.55: Propagation of waves in z-direction.

Chapter 6

Conclusions

In this thesis an extension to the SAGE algorithm has been proposed to make the algorithm suitable for high accuracy parameter estimation in UWB radio channels. The approach relies on established signal models using SIMO antenna configurations for the estimation of delays, incident azimuth angles, elevation angles, and complex amplitudes of deterministic MPCs.

The underlying signal model, as well as the unmodified wideband SAGE algorithm have been discussed. The problem of multiple detection of waves has been examined, which occurs when applying the unmodified SAGE algorithm to UWB measurement data. A simple time gating approach that depends on antenna array dimensions has been introduced to mitigate the effects of this problem.

To investigate the results obtained by the extended SAGE, the algorithm has been applied to measurement data acquired in environments that vary in size, as well as amount of inventory, and therefore show different channel characteristics.

In the first part of the measurement analysis, the algorithm has been applied to data arising from 2-dimensional antenna arrays in the x-y-plane, positioned in a sparsely furnished office. For both measurement scenarios in this office the channel is characterized by strong deterministic MPCs and low to medium stochastic noise. Because of the nature of the measurements and since elevation angles could be expected to be mainly around $0°$, the estimation of elevation angles has been neglected. Results demonstrate that the algorithm is capable of correctly extracting deterministic MPCs from the measurement data. It has been shown that a good approximation of the channel can be achieved by reconstructing the received signals with the estimated wave parameters. An illustration of the detected MPCs propagating through several antenna arrays suggests path tracking potential. The results were equally satisfying for several examined bandwidths.

In the second part of the measurement analysis, measurements that were taken in a lecture hall and in a computer lab, respectively, have been investigated. Estimation of elevation angles has been considered in this part of the thesis. Both measurement environments exhibit medium to high levels of stochastic noise and weak deterministic MPCs. In addition to that, the data provided only poor azimuth angle resolution due to the chosen antenna array geometry. The results therefore show that the extended SAGE is able to extract deterministic MPCs, but under these circumstances, as has been illustrated by channel reconstruction, not very accurately for all considered bandwidths.

The obtained results confirm that the simple time gating extension eliminates the need for more complex delay-and-sum beamforming. Furthermore can be concluded that the performance of the proposed algorithm is heavily dependent on the channel characteristics. Strong, temporally not too closely-spaced deterministic MPCs have been correctly and accurately detected. A high noise level as well as weak, temporally close MPCs pose a problem to the algorithm. Another important factor is the choice of antenna array configuration. The time gating approach lowers the temporal resolution significantly for arrays with large dimensions. Small array dimensions on the other hand lower the resolution of the incident angles. Hence, an appropriate antenna array configuration has to be selected carefully, in order not to affect performance. Since the algorithm has delivered satisfying results for all of the considered bandwidths, the ultimate choice of bandwidth can be left open to meet other demands of particular applications.

Bibliography

[Cap69] J. Capon. High-resolution frequency-wavenumber spectrum analysis. *Proceedings of the IEEE*, 57(8):1408 – 1418, Aug. 1969.

[CPD09] Jean-Marc Conrat, Patrice Pajusco, and Albin Dunand. On the use of panoramic photography for understanding propagation channel physical phenomena. In *9th COST2100 Management Committee Meeting*, TD(09)901, Vienna, Austria, Sept. 2009.

[CSW02] R.J.-M. Cramer, R.A. Scholtz, and M.Z. Win. Evaluation of an ultra-wideband propagation channel. *Antennas and Propagation, IEEE Transactions on*, 50(5):561–570, May 2002.

[dAUK04] G.T.F. de Abreu, T. Uefuji, and R. Kohno. Parameter estimation of UWB-IR signals using array antennas with hermite-hadamard orthogonal filters. In *Proc. IEEE 7th Wireless Personal Multimedia Conference (WPMC'04)*, pages 288–292, Sept. 2004.

[DLR77] A. P. Dempster, N. M. Laird, and D. B. Rubin. Maximum likelihood from incomplete data via the EM algorithm. *Journal of the Royal Statistical Society, Series B*, 39(1):1–38, 1977.

[FDHT96] B.H. Fleury, D. Dahlhaus, R. Heddergott, and M. Tschudin. Wideband angle of arrival estimation using the SAGE algorithm. In *Spread Spectrum Techniques and Applications Proceedings, 1996., IEEE 4th International Symposium on*, volume 1, Sept. 1996.

[FH94] J.A. Fessler and A.O. Hero. Space-alternating generalized expectation-maximization algorithm. *Signal Processing, IEEE Transactions on*, 42(10):2664–2677, Oct. 1994.

[FRB97] J. Fuhl, J.-P. Rossi, and E. Bonek. High-resolution 3-d direction-of-arrival determination for urban mobile radio. *Antennas and Propagation, IEEE Transactions on*, 45(4):672–682, April 1997.

[FTH+99] B.H. Fleury, M. Tschudin, R. Heddergott, D. Dahlhaus, and K. Ingeman Pedersen. Channel parameter estimation in mobile radio environments using the SAGE algorithm. *Selected Areas in Communications, IEEE Journal on*, 17(3):434–450, March 1999.

[FW88] M. Feder and E. Weinstein. Parameter estimation of superimposed signals using the EM algorithm. *Acoustics, Speech and Signal Processing, IEEE Transactions on*, 36(4):477–489, April 1988.

[GTG+05] S. Gezici, Zhi Tian, G.B. Giannakis, H. Kobayashi, A.F. Molisch, H.V. Poor, and Z. Sahinoglu. Localization via ultra-wideband radios: a look at positioning aspects for future sensor networks. *Signal Processing Magazine, IEEE*, 22(4):70–84, July 2005.

[HT03a] K. Haneda and J. Takada. High-resolution estimation of NLOS indoor MIMO channel with network analyzer based system. In *Personal, Indoor and Mobile Radio Communications, 2003. PIMRC 2003. 14th IEEE Proceedings on*, volume 1, pages 675–679 Vol.1, Sept. 2003.

[HT03b] K. Haneda and J.-I. Takada. An application of SAGE algorithm for UWB propagation channel estimation. In *Ultra Wideband Systems and Technologies, 2003 IEEE Conference on*, pages 483–487, Nov. 2003.

[IMS] IMST GmbH. Carl-Friedrich-Gauss-Str. 2, 47475 Kamp-Lintfort, Germany, http://www.imst.com.

[Kay93] S.M. Kay. *Fundamentals of Statistical Signal Processing: Estimation Theory*. Prentice-Hall, Inc., Upper Saddle River, NJ, USA, 1993.

[KP02] J. Kunisch and J. Pamp. Measurement results and modeling aspects for the UWB radio channel. In *Ultra Wideband Systems and Technologies, 2002. Digest of Papers. 2002 IEEE Conference on*, pages 19–23, 2002.

[KP03a] J. Kunisch and J. Pamp. An ultra-wideband space-variant multipath indoor radio channel model. In *Ultra Wideband Systems and Technologies, 2003 IEEE Conference on*, pages 290–294, Nov. 2003.

[KP03b] J. Kunisch and J. Pamp. UWB radio channel modeling considerations. In *Proc. ICEAA 2003*, Turin, Sept. 2003.

[LKV07] T.C.-K. Liu, D.I. Kim, and R.G. Vaughan. A high-resolution, multi-template deconvolution algorithm for time-domain uwb channel characterization. *Electrical and Computer Engineering, Canadian Journal of*, 32(4):207 –213, 2007.

[Mol09] A.F. Molisch. Ultra-wide-band propagation channels. *Proceedings of the IEEE*, 97(2):353–371, Feb. 2009.

[Moo96] T.K. Moon. The expectation-maximization algorithm. *Signal Processing Magazine, IEEE*, 13(6):47–60, Nov. 1996.

[PFM97] K.I. Pedersen, B.H. Fleury, and P.E. Mogensen. High resolution of electromagnetic waves in time-varying radio channels. In *Personal, Indoor and Mobile Radio Communications, 1997. 'Waves of the Year 2000'. PIMRC '97., The 8th IEEE International Symposium on*, volume 2, pages 650–654 vol.2, Sept. 1997.

[PNG08] A. Paulraj, R. Nabar, and D. Gore. *Introduction to Space-Time Wireless Communications*. Cambridge University Press, New York, NY, USA, 2008.

[Sch86] R. Schmidt. Multiple emitter location and signal parameter estimation. *Antennas and Propagation, IEEE Transactions on*, 34(3):276 – 280, March 1986.

[SPS] Signal Processing and Speech Communication Laboratory, Inffeldgasse 12, 8010 Graz, Austria, http://www.spsc.tugraz.at/.

[tug] Graz University of Technology, Rechbauerstrasse 12, 8010 Graz, Austria, http://portal.tugraz.at/portal/page/portal/TU_Graz.

[Unt09] Christian Unterkofler. Reflection Characteristics in UWB Propagation Environments. Master's thesis, Signal Processing and Speech Communication Laboratory, Graz University of Technology, Austria, May 2009.

[Van02] H.L. Van Trees. *Optimum Array Processing. Part IV of Detection, Estimation, and Modulation Theory*. Wiley-Interscience, John Wiley & Sons, Inc, New York, USA, 2002.

[why] "whyless.com – the open mobile access network," IST-2000-25197, http://www.whyless.org, 2006.